Polymer Composites

WILEY | spe INSPIRING PLASTICS PROFESSIONALS

RESEARCH ARTICLE OPEN ACCESS

Effect of $Ti_3C_2T_x$ MXene Incorporation on the Mechanical Performance and Microstructural Characteristics of Bulk Molding Compound Composites

Bilge Yılmaz[1] | Cemal Meran[2] | Cahit Bilgi[3]

[1]Vocational School, Department of Mechanical and Metal Technologies, Istanbul Gelisim University, Istanbul, Türkiye | [2]Faculty of Engineering, Department of Mechanical Engineering, Pamukkale University, Denizli, Türkiye | [3]Department of Aircraft Technologies, Istanbul University-Cerrahpaşa, Istanbul, Türkiye

Correspondence: Bilge Yılmaz (biyilmaz@gelisim.edu.tr)

Received: 25 May 2026 | **Revised:** 17 July 2026 | **Accepted:** 27 July 2026

Keywords: bulk molding compound | mechanical performance | microstructural characterization | polymer composites | $Ti_3C_2T_x$ MXene

ABSTRACT

Bulk molding compound (BMC) composites are widely used in engineering applications; however, improving their mechanical response through low-content nanoscale modification remains challenging for highly filled thermoset molding systems. In this study, $Ti_3C_2T_x$ MXene was incorporated into an industrial BMC formulation under unchanged compression-molding conditions to investigate its influence on mechanical and microstructural characteristics. The unmodified BMC and composites containing 0.238, 0.476, and 0.714 wt.% MXene were characterized using tensile testing, Izod impact testing, Shore D hardness, FTIR, XRD, TEM, SEM, and SEM–EDS. $Ti_3C_2T_x$ MXene addition improved the mechanical response within the investigated low-content range. The average tensile strength increased from 14.24 MPa for unmodified BMC to 24.00 MPa for the 0.714 wt.% MXene-added composite, a 68.6% improvement. The tensile modulus increased from 7.85 to 10.14 GPa, absorbed impact energy increased by up to 52.6%, and Shore D hardness increased from 70.6 to 75.8. TEM provided local evidence of MXene-related layered and partially overlapped regions, while SEM–EDS supported Ti-containing MXene-related regions in powder mixtures and molded bulk composites. BMC/MXene-0.71 exhibited the highest average mechanical values, whereas BMC/MXene-0.48 showed a more repeatable mechanical response and a comparatively balanced distribution tendency.

1 | Introduction

Bulk molding compound (BMC) composites are industrial thermoset molding materials composed of polymer resin matrices, chopped fiber reinforcements, mineral fillers, and functional additives [1–5]. Owing to their dimensional stability, corrosion resistance, moldability, and suitability for high-volume molding processes, BMC and related molded thermoset composites are used in molded electrical housings, circuit breaker components, motor and sensor parts, automotive under-hood components, corrosion-resistant molded plates, structural covers, and other functional molded parts [1–3, 5, 6]. Conductive BMC-type composite systems are also used or considered for molded plate-type components in electrochemical and fuel-cell-related applications, where the final part must satisfy both mechanical and functional requirements such as dimensional stability, conductivity, corrosion resistance, and mold-fill capability [7–12]. In transportation-oriented applications, polymer composite materials are also discussed for railway vehicle structures, where lightweight design, durability, and mechanical reliability are important design criteria [6]. For these application areas, improving the mechanical response of BMC composites without disrupting their established industrial molding route remains an important materials-design issue [8, 9, 13].

Highlights

- Low-content $Ti_3C_2T_x$ MXene was added to industrial BMC composites.
- Tensile strength increased by 68.6% at 0.714 wt.% MXene.
- Impact energy improved by up to 52.6% with MXene addition.
- TEM and SEM–EDS supported the identification of MXene-related regions.

In highly filled molded thermoset composites, the mechanical response is not governed only by the polymer matrix, but by the combined effects of fiber length, filler type, solid-particle packing, mold flow, matrix–filler contact, defect formation, and local microstructural continuity [2, 14, 15]. Previous BMC studies have shown that changes in fiber length and filler configuration can markedly influence tensile strength, tensile modulus, and impact resistance, even when the same molding equipment or a similar processing route is maintained [13–15]. In conductive or plate-type thermoset composite systems, additional filler-related issues such as reduced flowability, nonuniform packing, void formation, and molding defects may further affect the final part quality [7–9]. These effects are especially relevant for molded electrical, automotive, structural-cover, corrosion-resistant plate, and fuel-cell plate applications, where tensile resistance, impact tolerance, hardness stability, and dimensional reliability must be preserved after molding [1, 12, 13]. For this reason, introducing an additional nanoscale phase into an already highly filled BMC formulation requires attention not only to the potential reinforcing effect of the additive, but also to process compatibility, microstructural heterogeneity, and repeatability of the mechanical response [16–18].

Nanoscale and layered filler systems have been widely investigated to modify the mechanical, fracture-related, thermal, electrical, and tribological behavior of polymer composites [19–22]. Carbon nanotubes, carbon black, expanded graphite, graphene nanoplatelets, graphene oxide, layered silicates/nanoclay, hexagonal boron nitride, molybdenum disulfide, and MXene represent different filler families with distinct dimensionality, aspect ratio, surface chemistry, stiffness, conductivity, and compatibility with polymer matrices [22–26]. One-dimensional carbon nanotubes and particulate carbon-based fillers can contribute to mechanical or functional performance when their distribution and matrix contact are controlled, whereas graphene-based nanoplatelets and other layered fillers are frequently associated with large interfacial area, crack-path modification, barrier-related effects, and multifunctional property development [27–32]. However, the contribution obtained from these fillers is not automatic; it is strongly affected by dispersion quality, orientation state, addition level, matrix compatibility, and the prevention of agglomeration, restacking, or local filler-rich regions [16–18, 33–35]. In highly filled BMC systems, these factors become even more critical because the matrix already contains multiple solid constituents before the introduction of a secondary nanoscale additive [7–9, 18].

Among emerging two-dimensional nanomaterials, $Ti_3C_2T_x$ MXene is of particular interest for polymer composite modification because of its layered transition-metal carbide structure, high aspect ratio, large accessible surface area, electrical conductivity, and surface terminations such as —O, —OH, and —F [36–38]. These structural and surface characteristics distinguish $Ti_3C_2T_x$ MXene from many conventional carbon-based or clay-type fillers by providing a chemically active and tunable surface that may support matrix–filler contact in polymer composites [22, 26, 39, 40]. Experimental and computational studies on MXene/polymer systems have reported that the mechanical contribution of $Ti_3C_2T_x$ MXene depends on interfacial interaction, nanosheet distribution, matrix compatibility, and the ability of MXene-related regions to participate in load-bearing or crack-interaction processes [39–41]. Direct measurements on $Ti_3C_2T_x$ MXene monolayers also show that MXene nanosheets possess high intrinsic elastic modulus and tensile strength, which supports their potential use as mechanically relevant two-dimensional additives [42]. At the same time, MXene nanosheets may undergo restacking, partial agglomeration, or local concentration when the addition amount and processing route are not properly controlled [18, 43–45]. Therefore, in an already highly filled BMC formulation, $Ti_3C_2T_x$ MXene addition should be evaluated through a low-content and process-compatible approach rather than through a maximum-addition strategy [7–9, 18].

Recent MXene/polymer studies have expanded from basic nanocomposite systems toward mechanically, thermally, electrically, tribologically, and multifunctionally modified polymer structures [46–51]. $Ti_3C_2T_x$ MXene has been investigated in Elium composites, carbon fabric/epoxy laminates, PVA nanocomposites, MXene/CNT hybrid epoxy systems, epoxy coatings, structural epoxy adhesives, short-carbon-fiber/epoxy composites, wrinkled-MXene/epoxy systems, PLA/PU shape-memory blends, and low-content epoxy formulations [41, 52–60]. These studies show that the contribution of MXene is strongly formulation-dependent and may involve tensile or flexural improvement, fracture-toughness development, thermal or electrical functionality, EMI shielding, wear resistance, adhesive performance, hydrothermal durability, or self-sensing capability depending on matrix type, MXene addition amount, surface state, and dispersion route [40, 41, 52–56, 58, 60]. Recent review papers also emphasize that MXene/polymer composites should be interpreted in terms of architecture, surface modification, interfacial contact, delamination/restacking behavior, multifunctionality, and life-cycle or scalability considerations [18, 43, 46, 50, 51]. However, the majority of these studies have focused on epoxy, thermoplastic, elastomeric, adhesive, coating, or fiber-reinforced composite systems rather than industrial BMC formulations [41, 52, 53, 55, 56, 59, 60]. Therefore, the response of highly filled BMC composites to low-content $Ti_3C_2T_x$ MXene addition remains insufficiently defined, particularly in terms of tensile strength, impact energy absorption, Shore D hardness, structural characterization, and Ti-containing MXene-related regions after compression molding [1, 2, 8, 9, 18, 26, 48].

Although BMC and related molded thermoset composites are already used in component-level applications such as electrical housings, automotive under-hood parts, corrosion-resistant

molded plates, structural covers, and conductive plate-type components, most BMC-focused studies have examined the effects of fiber length, filler type, aging, molding defects, flowability, formability, or bipolar-plate processing rather than $Ti_3C_2T_x$ MXene addition as a secondary nanoscale modification [1, 2, 7–9, 13–15]. In parallel, recent MXene/polymer studies have mainly addressed epoxy, thermoplastic, elastomeric, coating, adhesive, and fiber-reinforced systems, where MXene has been used to modify tensile, flexural, fracture-related, tribological, electrical, EMI-shielding, or durability-related responses [41, 52–60]. Therefore, the behavior of highly filled industrial BMC formulations containing low amounts of $Ti_3C_2T_x$ MXene under unchanged compression-molding conditions has received comparatively limited attention [7, 8, 18, 26, 46]. This limitation is particularly relevant for molded BMC components that are expected to maintain tensile resistance, impact-energy absorption, surface hardness, dimensional reliability, and microstructural consistency after molding [1, 2, 9, 13]. In this context, evaluating mechanical properties together with FTIR, XRD, TEM, SEM, and SEM–EDS observations can provide a broader and more cautious basis for discussing the relationship between low-content $Ti_3C_2T_x$ MXene addition, structural features, Ti-containing MXene-related regions, and the mechanical response of industrial BMC composites [18, 21, 26, 40].

For this purpose, the characterization framework should distinguish between different levels of mechanical and microstructural information rather than treating all tests as evidence of the same reinforcement mechanism [18, 21, 26]. Tensile testing provides information on load-bearing response, tensile strength, modulus development, and specimen-to-specimen variability, while Izod impact testing reflects the ability of the composite to absorb energy under sudden fracture conditions [1, 13–15]. Shore D hardness, in contrast, represents a localized indentation response and should be interpreted as a surface-level mechanical indicator rather than a direct measure of bulk toughness or tensile reinforcement [61, 62]. Spectroscopic and structural techniques such as FTIR and XRD can provide supporting information on functional group-related features and diffraction characteristics, although weak or overlapping signals may occur because of the low MXene content and the carbonaceous, highly filled nature of the BMC formulation [7, 11, 26, 37, 38]. TEM observations can support the local evaluation of layered MXene-related regions, whereas SEM and SEM–EDS can provide powder-state and compression-molded bulk morphological information together with elemental evidence for Ti-containing MXene-related regions over selected observation areas [16, 18, 24, 40]. Interpreting these methods together provides a more balanced basis for discussing the relationship between $Ti_3C_2T_x$ MXene addition, structure-related features, and mechanical response without assigning the observed property changes to a single unverified mechanism [16, 18, 26, 46].

Based on this background, the present study investigates the mechanical performance and microstructural characteristics of an industrial BMC system modified with low amounts of $Ti_3C_2T_x$ MXene under unchanged compression-molding conditions [1, 8, 18, 26]. The unmodified BMC was compared with three MXene-added BMC groups containing 0.238, 0.476, and 0.714 wt.% $Ti_3C_2T_x$ MXene. The study evaluates tensile strength and tensile modulus, Izod impact energy, Shore D hardness, FTIR/XRD/TEM-supported structural features, powder-state and compression-molded bulk SEM morphology, and SEM–EDS-supported Ti-containing MXene-related regions within the same experimental framework [21, 26, 40, 61, 63, 64]. The novelty of this work is not based on maximizing the MXene amount, but on examining whether a low-content $Ti_3C_2T_x$ MXene modification can improve the mechanical response of an already highly filled industrial BMC formulation without changing the established molding route [7, 9, 13, 52, 60]. By connecting mechanical results with spectroscopic, structural, and microstructural observations, this study provides a process-compatible assessment of $Ti_3C_2T_x$ MXene addition in BMC composites and addresses a gap between BMC-based molded thermoset studies and recent MXene-modified polymer composite research [1, 2, 46, 48, 50].

2 | Materials and Methods

2.1 | Materials

Bulk molding compound (BMC) was used as the base thermoset molding material in this study. The BMC material was selected from an industrial formulation to keep the experimental design close to practical compression-molding conditions [1, 2, 7]. According to the supplier-provided technical information, the BMC is intended for molded plate-type components requiring electrical conductivity, corrosion resistance, dimensional stability, mold-fill capability, and cost-effective production. The supplier-reported typical tensile strength of the as-molded BMC is 15 MPa. The supplier-disclosed safety information describes the material as a carbonaceous composite mixture containing synthetic graphite and other carbon-containing constituents. The BMC was used as received, without any chemical or physical pre-treatment before MXene addition [7–9].

Commercial $Ti_3C_2T_x$ MXene powder was used as the secondary nanoscale additive. The powder was supplied by Nanografi Nanotechnology, Türkiye, with the product code NG10MPW1491. According to the supplier-provided data sheet, the MXene powder had a minimum purity of 98%, a particle size range of 2–20 μm, and a multilayer $Ti_3C_2T_x$ structure containing —OH, —O, and —F surface terminations. The supplier-declared elemental composition includes Ti, C, F, and O as the main constituents. The MXene powder was added to the BMC formulation without additional chemical surface functionalization [26, 37, 38].

2.2 | Composite Preparation, Compression Molding, and Specimen Production

All composite groups were prepared using a constant initial batch mass of 420 g to provide a direct comparison between the unmodified BMC and the MXene-added BMC formulations. The unmodified BMC group consisted of 420 g of BMC. The MXene-added groups were prepared by replacing part of the BMC mass with $Ti_3C_2T_x$ MXene powder at 1, 2, and 3 g, corresponding to

TABLE 1 | Initial formulation of BMC and MXene-added BMC composites.

Sample group	BMC mass (g)	MXene mass (g)	MXene content (wt.%)
BMC	420	0	0
BMC/MXene-0.24	419	1	0.238
BMC/MXene-0.48	418	2	0.476
BMC/MXene-0.71	417	3	0.714

BMC/MXene-0.24, BMC/MXene-0.48, and BMC/MXene-0.71, respectively. Accordingly, the MXene contents were calculated as 0.238, 0.476, and 0.714 wt.% based on the initial 420 g batch mass. The formulation details are given in Table 1.

The selected MXene contents were deliberately restricted to a low-content range because the purpose of this study was not to determine the maximum possible MXene concentration, but to evaluate whether measurable mechanical improvement could be achieved in an industrial BMC system without changing the established compression-molding route. This consideration is important for conductive BMC and plate-type thermoset composite systems, where filler content, mixing behavior, mold flow, formability, dimensional stability, and production repeatability should be considered together [7, 9–13]. The selected additions of 1, 2, and 3 g correspond to 0.238, 0.476, and 0.714 wt.% with respect to the initial 420 g batch mass. This sub-1 wt.% range was selected to preserve the process-compatible character of the BMC formulation while examining the possible mechanical contribution of $Ti_3C_2T_x$ MXene at very low contents. Excessive addition of a secondary nanoscale filler may affect dry mixing behavior, local filler packing, molding flow, defect formation tendency, cost efficiency, and the tendency for local nanosheet restacking or accumulation. Therefore, higher MXene contents would require a separate processability-oriented optimization study rather than a direct extension of the present low-content comparison [18, 43–45, 50, 52, 53].

$Ti_3C_2T_x$ MXene powder was introduced into the BMC compound without additional chemical surface treatment. In this study, this step was considered as an alloying-type physical incorporation process, in which the MXene powder was mechanically integrated into the industrial BMC formulation before compression molding. The BMC/MXene mixtures were prepared using a mechanical mixing process at 3000 rpm for 300 s. The same mixing speed, mixing duration, and preparation route were applied to all MXene-containing groups in order to maintain comparable processing conditions among the formulations. Since both the BMC matrix and $Ti_3C_2T_x$ MXene powder were dark-colored, visual inspection was not considered sufficient to evaluate the distribution state of MXene within the mixture. Therefore, the preparation route was standardized for all formulations, and the effect of MXene content was evaluated under identical mixing and molding conditions [16, 18].

The sample preparation, specimen fabrication, and characterization workflow of the $Ti_3C_2T_x$ MXene-added BMC composites is presented in Figure 1.

As shown in Figure 1, the workflow includes preparation of the BMC raw material, weighing of $Ti_3C_2T_x$ MXene powder, compression molding, production of composite plates, preparation of specimens by water-jet cutting, and subsequent mechanical, spectroscopic, structural, and microstructural characterization.

After mixing, the BMC and BMC/MXene mixtures were processed by industrial compression molding using an Engel Insert 160 press machine. All plates were produced using the same mold geometry and the same processing parameters. Before molding, the mold surfaces were cleaned and treated with a silicone-based mold release agent to facilitate demolding and preserve the molded plate surface. The pressing force was 1600 kN, and the pressing time was kept constant at 250 s. The upper and lower mold temperatures were set to 130°C and 165°C, respectively. These conditions were kept constant across all groups so that comparisons among the formulations would not be affected by intentionally varied molding parameters.

The compression-molded plates had approximate dimensions of 130 × 270 mm and an initial thickness of approximately 7 mm. After molding, the plates were machined to a final thickness of 3.2 mm before specimen extraction. The MXene content was expressed according to the initial batch composition rather than the final mass of the machined specimens, because material removal during thickness adjustment was applied after plate production and was not part of the formulation stage. This formulation-based normalization allowed the MXene-added groups to be compared using the same initial preparation basis [7–9].

Final test and characterization specimens were obtained from the thickness-adjusted plates by water-jet cutting and representative sampling. Tensile specimens were prepared according to ASTM D638 Type V geometry, with a final specimen thickness of 3.2 mm, an overall length of approximately 63.5 mm, a gauge length of approximately 7.62 mm, and a narrow section width of approximately 3.2 mm [63]. Izod impact specimens were prepared according to ASTM D256 with nominal dimensions of approximately 63.5 × 12.7 × 3.2 mm [64]. Shore D hardness specimens were prepared with approximate dimensions of 20 × 20 × 3.2 mm [61]. Representative material portions were also reserved from each composite group for FTIR, XRD, and TEM analyses to evaluate spectroscopic, structural, and local layered-region features within the same formulation set. For SEM–EDS characterization, representative circular specimens with an approximate diameter of 10 mm were prepared from each composite group. The same machining, cutting, and sampling route was applied to all groups to maintain dimensional and preparation comparability and to avoid specimen preparation-related differences as an additional source of variation. The plate thickness adjustment and specimen allocation route for mechanical, spectroscopic, structural, and microstructural characterization is schematically shown in Figure 2.

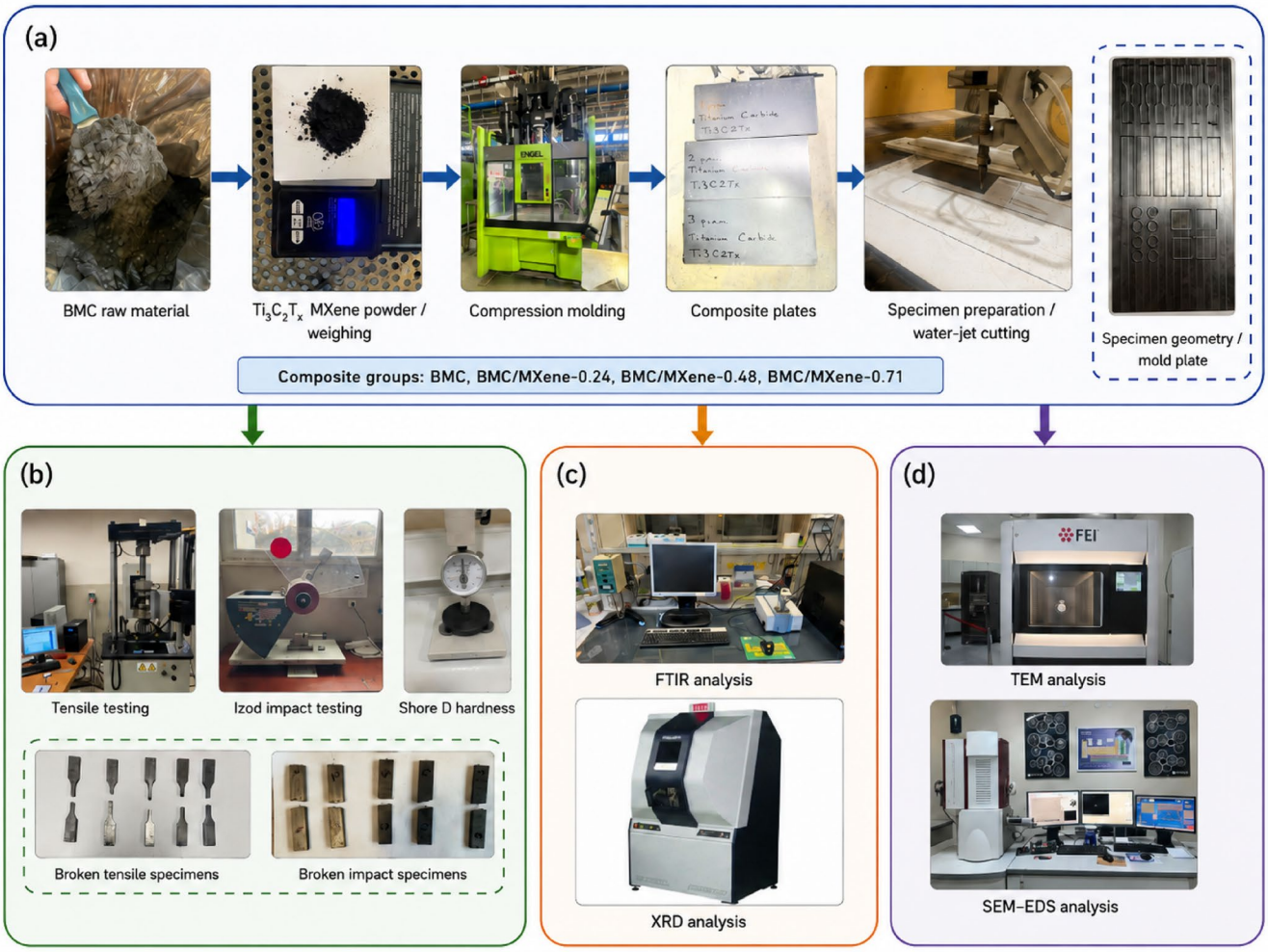

FIGURE 1 | Experimental workflow for $Ti_3C_2T_x$ MXene-added BMC composites: (a) sample preparation and specimen fabrication, (b) mechanical testing, (c) FTIR and XRD analyses, and (d) TEM and SEM–EDS characterization.

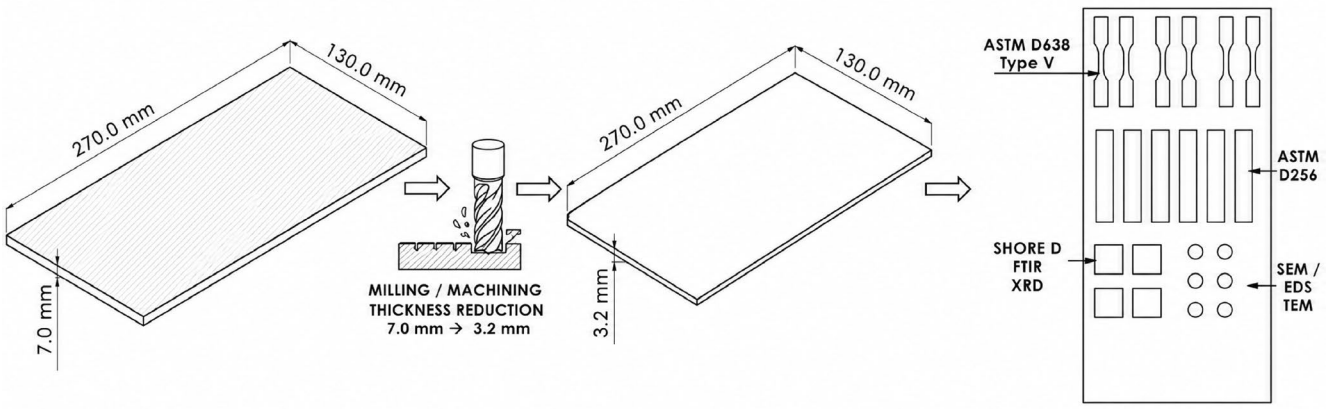

FIGURE 2 | Plate thickness adjustment and specimen allocation for mechanical, spectroscopic, structural, and microstructural characterization.

2.3 | Mechanical, Morphological, and Microstructural Characterization

Mechanical, morphological, and microstructural characterization was carried out using the same comparative framework for the BMC, BMC/MXene-0.24, BMC/MXene-0.48, and BMC/MXene-0.71 groups. Tensile testing, Izod impact testing, and Shore D hardness measurements were used to evaluate different aspects of the mechanical response. FTIR and XRD analyses were included as complementary spectroscopic and structural methods, while TEM, SEM, and SEM–EDS observations were used to support the evaluation of MXene-related layered features,

powder-state and compression-molded bulk morphology, and Ti-containing MXene-related regions. The methods were used in combination since no individual test was considered sufficient to explain the observed mechanical changes [18, 21, 26].

Tensile tests were performed using an Instron 8801 universal testing machine according to ASTM D638 Type V specimen geometry. Five specimens were tested for each composite group, and the tensile stress–strain response of each specimen was recorded; the ultimate tensile strength was determined from the maximum stress value of each curve [63]. The tensile modulus was calculated from the initial linear region of each stress–strain curve by applying linear regression to the 0.05%–0.15% strain interval. Since the strain values were recorded in percent, they were converted to dimensionless strain before modulus calculation. The average tensile strength, average tensile modulus, and corresponding standard deviation values were calculated for each formulation [63].

Izod impact tests were conducted using a CEAST Resil Impactor device according to ASTM D256. Five impact specimens were tested for each group, and the absorbed impact energy values were recorded directly in joules [64]. The average absorbed impact energy and corresponding standard deviation values were calculated for each formulation. The impact results were used to compare the ability of the composites to absorb energy under sudden fracture conditions rather than to provide a direct measure of tensile reinforcement [64].

Shore D hardness measurements were performed using a Werka Shore D 446-100D hardness tester according to ASTM D2240-15. Five measurements were taken for each composite formulation, and the average Shore D hardness values were calculated [61]. Shore D hardness was evaluated as a localized surface indentation response and was therefore interpreted as a complementary surface-level mechanical indicator [61].

FTIR spectra of the BMC and MXene-added BMC composites were recorded using a Bruker Alpha-P FTIR spectrometer with OPUS software. The measurements were performed in transmission mode over the wavenumber range of 4000–400 cm^{-1} at a spectral resolution of 4 cm^{-1} under room-temperature conditions. FTIR analysis was used to compare the main absorption features of the BMC and BMC/MXene groups and to evaluate possible spectral changes associated with $Ti_3C_2T_x$ MXene addition [18, 26].

XRD analysis was performed using a Rigaku SmartLab X-ray diffractometer with Cu Kα radiation. The diffraction patterns of BMC, BMC/MXene-0.24, BMC/MXene-0.48, and BMC/MXene-0.71 were collected using the same measurement conditions. The full-range XRD patterns were evaluated between 3° and 90°, and the low-angle region between 3° and 10° was additionally enlarged to examine MXene-related low-angle diffraction features. XRD analysis was used to compare the main diffraction characteristics of the composite groups and to evaluate whether detectable structural changes appeared within the investigated low-content MXene range. Because the MXene contents were below 1 wt.% and the BMC formulation contained carbonaceous/graphitic filler phases, weak or overlapping MXene-related diffraction features were interpreted cautiously and in combination with TEM and SEM–EDS observations [65–68].

TEM analysis was carried out using an FEI TALOS F200S transmission electron microscope operated at 200 kV. Representative samples from the MXene-added BMC groups were examined under the same comparative framework. TEM observations were used to support the local evaluation of layered MXene-related regions, fringe-like contrast features, and possible local restacking or accumulation tendencies within selected observation areas [18, 43, 47].

SEM and SEM–EDS analyses were performed using a TESCAN MAIA3 XMU field-emission scanning electron microscope equipped with an Oxford X-Max 50 EDS detector. Representative powder-state and bulk specimens from each composite group were examined. SEM observations were used to evaluate the morphological features of the powder mixtures and molded bulk specimens. EDS elemental mapping and spectra were used to support the identification of Ti-containing MXene-related regions and to compare their distribution tendency among the MXene-added groups [16, 18, 21, 46].

3 | Results and Discussion

3.1 | Tensile Properties

The tensile behavior of the unmodified BMC and $Ti_3C_2T_x$ MXene-added BMC composites was evaluated using tensile stress–strain curves, ultimate tensile strength values, and tensile modulus values. The tensile stress–strain curves of the produced composite groups are presented in Figure 3, and the corresponding tensile strength and tensile modulus data are summarized in Table 2. The unmodified BMC specimens exhibited the lowest average tensile strength among all groups, with a value of 14.24 ± 1.06 MPa. This value is close to the supplier-reported typical tensile strength of the industrial BMC material, indicating that the reference specimens provided a reasonable baseline for evaluating the effect of $Ti_3C_2T_x$ MXene addition.

As shown in Figure 3, the unmodified BMC group exhibited lower stress levels than the MXene-added groups during tensile loading. With increasing $Ti_3C_2T_x$ MXene content, the stress response of the composites increased, particularly for the BMC/MXene-0.48 and BMC/MXene-0.71 groups. The highest stress levels were observed for BMC/MXene-0.71, whereas BMC/MXene-0.48 showed a more closely grouped tensile response among the five tested specimens. Therefore, the tensile curves indicate that MXene addition increased the stress-bearing response of the BMC composites at all three addition levels, although the degree of repeatability varied among the formulations.

The small fluctuations observed in some stress–strain curves should be considered in relation to the heterogeneous and highly filled nature of the industrial BMC system. BMC contains multiple solid constituents, including fiber, mineral filler, carbonaceous filler, and other formulation-related components. During tensile loading, local filler-rich regions, fiber/filler discontinuities, interfacial heterogeneity, fiber/matrix debonding, and early microdamage events may cause minor variations or local stress drops in the recorded stress response. Similar non-ideal

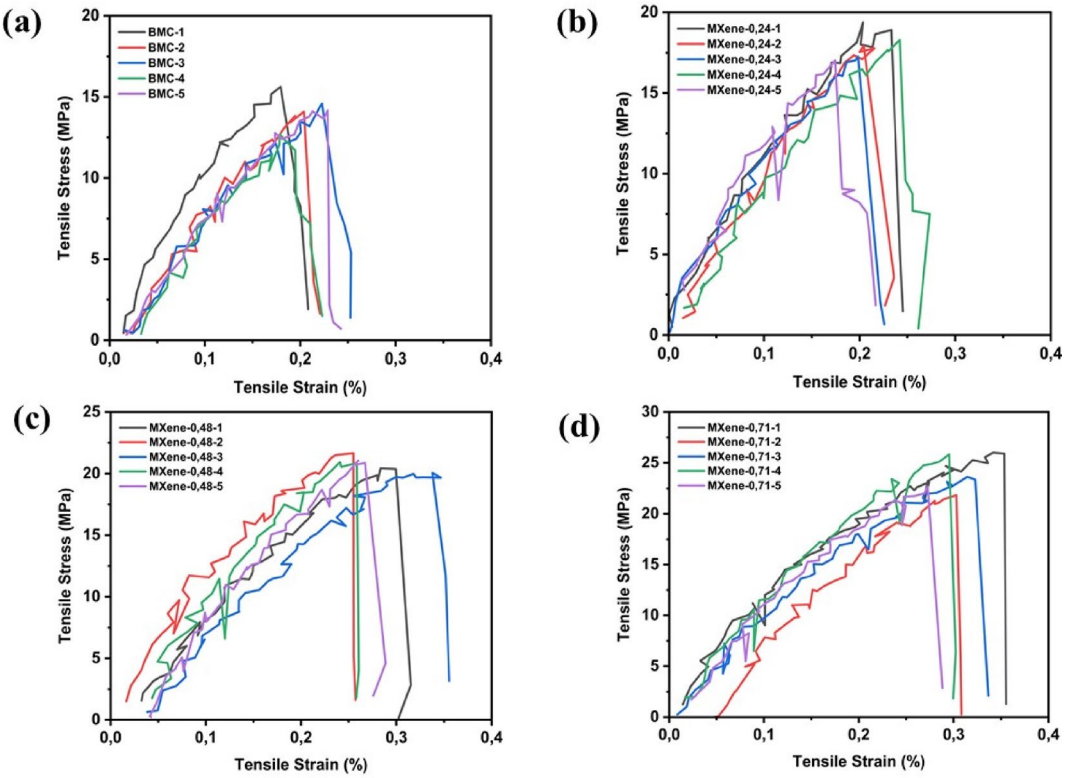

FIGURE 3 | Tensile stress–strain curves of (a) BMC, (b) BMC/MXene-0.24, (c) BMC/MXene-0.48, and (d) BMC/MXene-0.71 composites.

stress–strain responses and damage-related interpretations have been reported for glass-fiber-reinforced BMC systems, where tensile behavior was affected by fiber length, filler-rich microstructure, acoustic-emission-detected cracking, and SEM-observed fiber/matrix debonding. Comparable damage-related curve behavior has also been reported for closely related sheet molding compound systems under tensile loading, where acoustic-emission studies and viscoelastic-damage analyses associated non-linear or non-smooth tensile response with progressive internal cracking and fiber–matrix interfacial microcracking. Similar fluctuation-type features before final failure have also been shown in tensile curves of natural-fiber/polyester composites and were associated with progressive damage and partial fiber failure. In addition, the ASTM D638 Type V specimen geometry has a relatively small gauge section, which can make the measured response more sensitive to local heterogeneity within compression-molded BMC plates. Therefore, the fluctuations in Figure 3 were not interpreted as a separate deformation mechanism or instrumental error, but as an experimental feature associated with highly filled and heterogeneous compression-molded BMC composites [13–15, 69–71].

As listed in Table 2, the average tensile strength increased from 14.24 ± 1.06 MPa for unmodified BMC to 17.98 ± 0.93, 20.83 ± 0.62, and 24.00 ± 1.88 MPa for BMC/MXene-0.24, BMC/MXene-0.48, and BMC/MXene-0.71, respectively. These values correspond to tensile strength increases of 26.3%, 46.3%, and 68.6% compared with unmodified BMC. This trend shows that $Ti_3C_2T_x$ MXene addition contributed positively to the ultimate tensile strength of the BMC composites across the three MXene-added groups. However, the increase in tensile strength should not be attributed to a single confirmed reinforcement mechanism; rather, it may be associated with the combined effects of MXene-related regions, matrix–filler contact, local structural continuity, and changes in fracture progression during tensile loading.

In addition to tensile strength, tensile modulus values were calculated from the initial linear region of each stress–strain curve by applying linear regression to the 0.05%–0.15% strain interval. Since the strain values were recorded in percent, they were converted to dimensionless strain before modulus calculation. The average tensile modulus increased from 7.85 ± 0.35 GPa for unmodified BMC to 8.47 ± 0.67, 9.58 ± 0.75, and 10.14 ± 1.05 GPa for BMC/MXene-0.24, BMC/MXene-0.48, and BMC/MXene-0.71, respectively. These values correspond to modulus increases of 7.9%, 22.0%, and 29.1%. Compared with the tensile strength improvement, the modulus increase was more moderate, indicating that low-content $Ti_3C_2T_x$ MXene addition affected the initial stiffness response and the ultimate load-bearing response at different levels.

The distinction between tensile strength and tensile modulus is important for interpreting the mechanical response of the BMC/MXene composites. Tensile strength reflects the maximum stress-bearing capacity before fracture, whereas tensile modulus represents the initial stiffness response under small deformation. The more moderate increase in modulus suggests that the early-stage stiffness of the already highly filled BMC system was less sensitive to low-content MXene addition than the fracture-related tensile strength. This behavior is reasonable because the unmodified BMC already contains a high amount of solid constituents that contribute to the initial stiffness of the composite structure. The modulus data therefore

TABLE 2 | Tensile strength and tensile modulus values of BMC and MXene-added BMC composites.

Sample group	MXene content (wt.%)	Tensile strength values (MPa)	Average tensile strength (MPa)	SD (MPa)	Increasing ratio (%)	Tensile modulus values (GPa)	Average tensile modulus (GPa)	SD of tensile modulus (GPa)	Modulus increase ratio (%)
BMC	0	15.63, 14.10, 14.59, 12.69, 14.17	14.24	1.06	—	8.02, 7.57, 7.67, 8.39, 7.62	7.85	0.35	—
BMC/MXene-0.24	0.238	19.38, 17.94, 17.27, 18.29, 17.02	17.98	0.93	26.3	8.54, 9.59, 7.96, 8.24, 8.03	8.47	0.67	7.9
BMC/MXene-0.48	0.476	20.42, 21.67, 20.06, 20.93, 21.05	20.83	0.62	46.3	9.24, 9.01, 9.06, 9.77, 10.81	9.58	0.75	22.0
BMC/MXene-0.71	0.714	26.01, 21.81, 23.63, 25.85, 22.69	24.00	1.88	68.6	9.01, 11.35, 9.07, 10.55, 10.70	10.14	1.05	29.1

strengthen the mechanical comparison, but they carry no information about how the MXene is spatially distributed within the plate [39, 40, 42].

Among the MXene-added groups, BMC/MXene-0.48 had the lowest standard deviation in tensile strength (0.62 MPa). BMC/MXene-0.71 reached a mean tensile strength of 24.00 MPa with a standard deviation of 1.88 MPa. Its mean tensile modulus was 10.14 GPa, with a standard deviation of 1.05 GPa. The mean tensile response therefore increased with MXene content, whereas repeatability did not improve at the same rate.

Accordingly, the tensile data were discussed with reference to the FTIR, XRD, TEM, SEM, and SEM–EDS findings. Direct tensile measurements on $Ti_3C_2T_x$ MXene monolayers have shown that MXene nanosheets possess high intrinsic elastic modulus and tensile strength, which supports their potential mechanical relevance in polymer composites. Nevertheless, in the present BMC system, the actual contribution of MXene depends on its local distribution, matrix contact, and compatibility with the highly filled thermoset formulation after compression molding. For this reason, the tensile strength and modulus improvements were considered as evidence of improved mechanical response within the investigated formulation range, while the underlying structure–property relationship was evaluated further using FTIR, XRD, TEM, SEM, and SEM–EDS analyses in the following sections [18, 54].

3.2 | Impact Behavior

The impact behavior of the unmodified BMC and $Ti_3C_2T_x$ MXene-added BMC composites was evaluated using the absorbed impact energy values obtained from ASTM D256 impact testing. The individual and average impact energy values are summarized in Table 3, and the average absorbed impact energy values with standard deviations are presented in Figure 4. The unmodified BMC specimens exhibited the lowest average absorbed impact energy, with a value of 0.043 ± 0.005 J. The MXene-added groups showed higher absorbed impact energy values than the unmodified BMC, indicating that $Ti_3C_2T_x$ MXene addition affected the fracture-related energy absorption response at all three addition levels.

As shown in Table 3, the average absorbed impact energy increased to 0.055 ± 0.004 J for BMC/MXene-0.24, 0.063 ± 0.001 J for BMC/MXene-0.48, and 0.066 ± 0.004 J for BMC/MXene-0.71. These values correspond to improvements of approximately 27.4%, 46.0%, and 52.6%, respectively, compared with unmodified BMC. This increase indicates that $Ti_3C_2T_x$ MXene addition improved the fracture-related energy absorption response of the composite structure during sudden loading. However, the difference between BMC/MXene-0.48 and BMC/MXene-0.71 was limited, with only a small increase in average absorbed energy from 0.063 J to 0.066 J. Therefore, the impact response did not increase as strongly as the tensile strength at the highest MXene content.

As shown in Figure 4, the absorbed impact energy increased progressively with MXene incorporation. The lowest impact energy was observed for unmodified BMC, whereas the

TABLE 3 | Absorbed impact energy values of BMC and MXene-added BMC composites.

Sample group	MXene content (wt.%)	Impact energy values (J)	Average impact energy (J)	SD (J)	Increasing ratio (%)
BMC	0	0.036, 0.041, 0.045, 0.046, 0.047	0.043	0.005	—
BMC/MXene-0.24	0.238	0.052, 0.057, 0.056, 0.050, 0.059	0.055	0.004	27.4
BMC/MXene-0.48	0.476	0.062, 0.063, 0.061, 0.065, 0.063	0.063	0.001	46.0
BMC/MXene-0.71	0.714	0.070, 0.064, 0.062, 0.063, 0.069	0.066	0.004	52.6

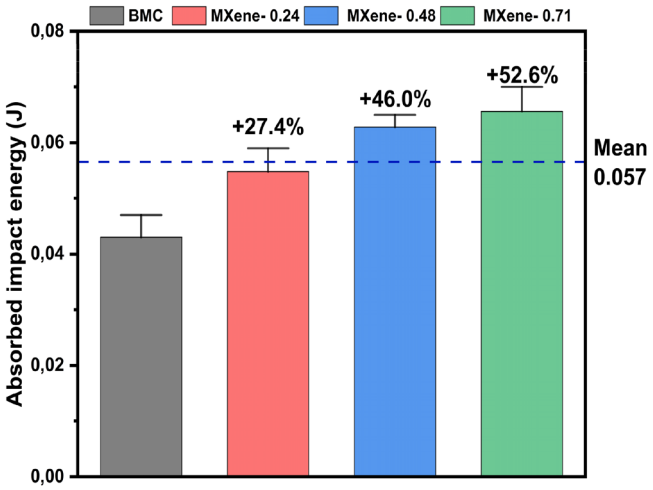

FIGURE 4 | Average absorbed impact energy and standard deviation of BMC and $Ti_3C_2T_x$ MXene-added BMC composites.

highest value was obtained for BMC/MXene-0.71. The BMC/MXene-0.48 and BMC/MXene-0.71 groups exhibited relatively close impact energy levels, indicating that the impact performance improvement became less pronounced at higher MXene contents. This limited additional gain at 0.714 wt.% MXene suggests that the impact-energy absorption response may approach saturation at the upper end of the tested composition interval.

In impact loading, the absorbed energy is influenced by crack initiation, crack propagation, local matrix deformation, filler-related heterogeneity, and fracture-path development. Therefore, the impact results should not be interpreted simply as a direct extension of the tensile strength trend. While tensile strength reflects the maximum stress-bearing capacity under quasi-static loading, the Izod impact test reflects the energy absorbed during a rapid fracture event [13]. For this reason, the impact behavior requires a separate interpretation from the tensile response.

The increase in absorbed impact energy may be associated with the presence of MXene-related regions that modify the fracture path and increase local energy dissipation during sudden loading. In nanofiller-containing polymer composites, layered or platelet-like fillers can contribute to crack deflection, crack-path tortuosity, and localized energy absorption when the filler-related regions are sufficiently involved in the fracture process [33, 52, 72–74]. In the present study, these effects are considered as possible explanations for the observed increase in impact energy rather than as directly proven fracture mechanisms.

Among the MXene-added groups, BMC/MXene-0.48 showed the lowest standard deviation in absorbed impact energy, while BMC/MXene-0.71 exhibited the highest average absorbed impact energy but with a larger standard deviation. This behavior is consistent with the tensile results in terms of repeatability: BMC/MXene-0.48 showed a more stable mechanical response, whereas the additional gain achieved by BMC/MXene-0.71 was accompanied by greater specimen-to-specimen variation. This suggests that increasing MXene content improved the average fracture-related energy absorption response, but the repeatability of this response may still depend on local distribution tendencies and microstructural heterogeneity.

The impact results indicate that low-content $Ti_3C_2T_x$ MXene addition improved the absorbed impact energy of the industrial BMC composites. However, the limited difference between the 0.48 and 0.71 wt.% MXene groups shows that the impact response should be evaluated not only by the highest average value, but also by the magnitude of the incremental improvement and the repeatability of the data. Accordingly, the integrated structure–property interpretation includes the impact results as well as the Shore D hardness, FTIR, XRD, TEM, SEM, and SEM–EDS observations.

3.3 | Shore D Hardness

Shore D hardness measurements were performed to evaluate the localized surface indentation response of the unmodified BMC and $Ti_3C_2T_x$ MXene-added BMC composites. The individual hardness values, average Shore D hardness values, standard deviations, and relative increases are given in Table 4, while the average hardness values with standard deviations are shown in Figure 5. The unmodified BMC specimens exhibited an average Shore D hardness of 70.6 ± 1.14. With $Ti_3C_2T_x$ MXene addition, the average hardness values increased progressively, reaching 72.4 ± 0.89 for BMC/MXene-0.24, 74.2 ± 1.30 for BMC/MXene-0.48, and 75.8 ± 0.84 for BMC/MXene-0.71.

TABLE 4 | Shore D hardness values of BMC and MXene-added BMC composites.

Sample group	MXene content (wt.%)	Hardness values (Shore D)	Average hardness (Shore D)	SD	Increasing ratio (%)
BMC	0	72, 71, 71, 69, 70	70.6	1.14	—
BMC/MXene-0.24	0.238	71, 73, 73, 72, 73	72.4	0.89	2.5
BMC/MXene-0.48	0.476	73, 76, 73, 75, 74	74.2	1.30	5.1
BMC/MXene-0.71	0.714	75, 76, 77, 76, 75	75.8	0.84	7.4

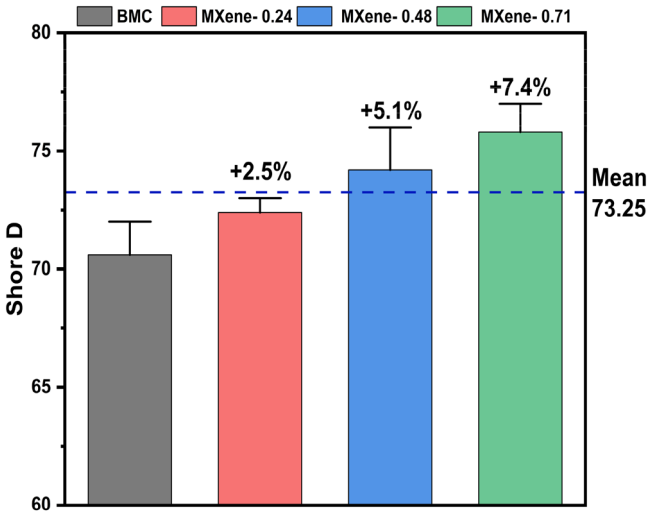

FIGURE 5 | Shore D hardness and standard deviation of BMC and $Ti_3C_2T_x$ MXene-added BMC composites.

Compared with the unmodified BMC, these values correspond to hardness increases of 2.5%, 5.1%, and 7.4%, respectively. The gradual increase in Shore D hardness indicates that the addition of $Ti_3C_2T_x$ MXene contributed to higher localized surface resistance at the tested addition levels. However, the magnitude of the hardness improvement was smaller than the increases observed in tensile strength and absorbed impact energy. This difference is important because Shore D hardness does not represent bulk tensile resistance or impact toughness; instead, it reflects the resistance of the near-surface region against localized indentation.

As shown in Figure 5, Shore D hardness increased progressively with MXene incorporation. The unmodified BMC group exhibited the lowest average hardness value, whereas the highest value was obtained for BMC/MXene-0.71. This trend suggests that the addition of $Ti_3C_2T_x$ MXene increased the localized indentation resistance of the BMC surface.

The more moderate hardness increase suggests that low-content MXene addition affected the surface-level indentation response of the BMC composites but did not change this response to the same extent as the fracture-related or load-bearing properties. This behavior may be related to the already rigid and highly filled nature of the industrial BMC formulation. Since the unmodified BMC contains multiple solid constituents, including carbonaceous and mineral filler phases, its baseline hardness is already relatively high. Therefore, the additional contribution of $Ti_3C_2T_x$ MXene to Shore D hardness is expected to appear as a gradual surface-level improvement rather than a large stepwise change.

Among the MXene-added groups, BMC/MXene-0.71 reached a mean Shore D hardness of 75.8, while BMC/MXene-0.24 showed the smallest hardness increase. The BMC/MXene-0.48 group provided an intermediate hardness value but showed the highest standard deviation among the MXene-added groups. These results indicate that the hardness response increased with MXene content, but local surface-level variability may still occur depending on the local distribution of filler-rich regions and the heterogeneous structure of the compression-molded BMC plates.

In this study, Shore D hardness was therefore interpreted as a complementary mechanical indicator rather than as direct evidence of a specific reinforcement mechanism. The observed hardness increase may be associated with the presence of rigid $Ti_3C_2T_x$ MXene-related regions and their possible contribution to local resistance against indentation [52, 62, 72]. Nevertheless, the hardness results alone do not confirm homogeneous MXene dispersion, direct interfacial strengthening, or improved bulk toughness. Accordingly, Shore D hardness was treated as one component of the integrated structure–property interpretation, which also incorporated the tensile, impact, FTIR, XRD, TEM, SEM, and SEM–EDS findings.

3.4 | FTIR Analysis

FTIR analysis was performed to obtain complementary spectroscopic information on the functional group-related features of the unmodified BMC and $Ti_3C_2T_x$ MXene-added BMC composites. The FTIR spectra of BMC, BMC/MXene-0.24, BMC/MXene-0.48, and BMC/MXene-0.71 are presented in Figure 6. The spectra were evaluated to compare the characteristic absorption features of the BMC system and to identify possible MXene-related spectral contributions at the selected addition levels.

The unmodified BMC spectrum exhibited broad and partially overlapping absorption features, which is expected for an industrial BMC formulation containing an unsaturated polyester/styrene-based matrix, carbonaceous filler, mineral filler, and other formulation-related constituents. The broad band observed around 3400–3300 cm^{-1} can be associated with O—H stretching vibrations

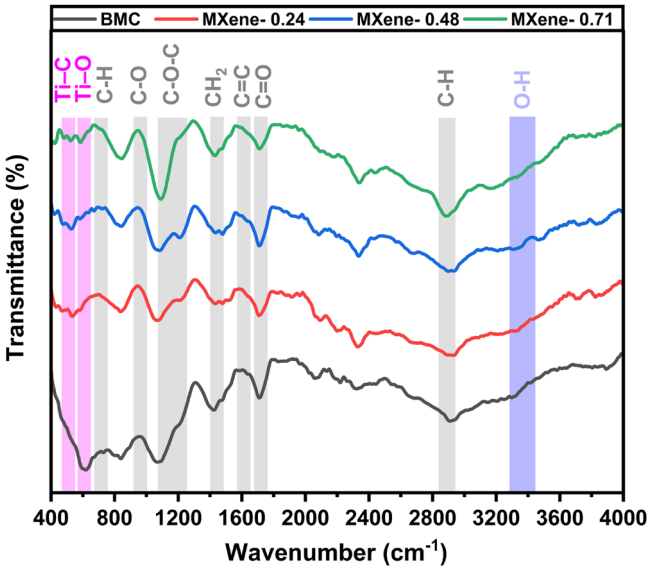

FIGURE 6 | FTIR spectra of unmodified BMC and $Ti_3C_2T_x$ MXene-added BMC composites.

originating from adsorbed water, residual hydroxyl end-groups of the unsaturated polyester resin, and hydroxyl-containing surface species of the mineral filler phases. In the MXene-added groups, the surface hydroxyl terminations of $Ti_3C_2T_x$ MXene are expected to contribute additionally to this region. The bands in the 2920–2850 cm^{-1} region correspond to C—H stretching vibrations of the unsaturated polyester/styrene matrix. The absorption band around 1730–1715 cm^{-1} is associated with C═O stretching of the ester groups in the unsaturated polyester resin, while the 1635–1600 cm^{-1} region can be assigned to aromatic C═C stretching of the styrene aromatic ring and possible absorbed-water contribution. The bands around 1455–1410 cm^{-1}, 1260–1150 cm^{-1}, 1120–1030 cm^{-1}, and 760–700 cm^{-1} are related to CH_2 bending, C—O—C stretching, C—O stretching, and aromatic C—H out-of-plane bending vibrations, respectively.

With the addition of $Ti_3C_2T_x$ MXene, the main absorption features of the BMC matrix were largely preserved, indicating that MXene addition did not cause a dominant chemical transformation of the polymer matrix at these low concentrations. However, slight spectral changes were observed in several regions. The O—H stretching region around 3400–3300 cm^{-1} became broader with increasing MXene content, which can be associated with hydrogen-bonding-type interactions involving MXene surface terminations and the surrounding polymer/filler environment. In addition, slight shifts and broadening were observed in the C═O and C—O/C—O—C related regions; these changes may indicate local interactions between ester groups of the polyester matrix and the surface functionalities of $Ti_3C_2T_x$ MXene.

The low-wavenumber region is particularly important for evaluating MXene-related spectral contributions. The bands around 650–550 cm^{-1} can be associated with Ti—O bending vibrations related to surface TiO_x species on $Ti_3C_2T_x$ MXene, while the 520–450 cm^{-1} region can be assigned to Ti—C vibrations of the $Ti_3C_2T_x$ MXene lattice. In the MXene-added composites, these low-wavenumber contributions became more distinguishable with increasing MXene content, supporting the identification of Ti-containing MXene-related spectral features in the BMC matrix. However, because the MXene contents were below 1 wt.% and the BMC formulation already contained carbonaceous and inorganic constituents, these MXene-related FTIR contributions were expected to be weak and partially overlapped with the BMC background.

The main FTIR band assignments and the effect of $Ti_3C_2T_x$ MXene incorporation are summarized in Table 5 [18, 26, 37–39].

Hydroxyl and oxygen-containing surface terminations may support local matrix–filler contact through polar or hydrogen-bonding-type interactions, while Ti—O and Ti—C related features provide complementary spectral support for $Ti_3C_2T_x$ MXene-related contributions. Nevertheless, the FTIR spectra alone do not confirm direct covalent bonding between MXene and the BMC matrix, nor do they prove homogeneous MXene dispersion throughout the composite structure.

Taken together, the FTIR results indicate that the main BMC spectral features were largely retained after $Ti_3C_2T_x$ MXene addition, while weak MXene-related low-wavenumber contributions and slight changes in O—H, C═O, and C—O/C—O—C related regions were observed. These spectral changes indicate possible functional group-related interactions and Ti-containing MXene-related features, while XRD, TEM, and SEM–EDS provide complementary structural, morphological, and elemental evidence.

3.5 | XRD Analysis

XRD analysis was performed to obtain complementary structural information on the unmodified BMC and $Ti_3C_2T_x$ MXene-added BMC composites. The full-range XRD patterns between 3° and 90° are shown in Figure 7a, while the enlarged low-angle region between 3° and 10° is presented in Figure 7b. The low-angle region was enlarged because the characteristic (002) reflection of multilayer $Ti_3C_2T_x$ MXene is generally observed at low 2θ values, whereas the full-range patterns of the present BMC system are dominated by the carbonaceous/graphitic constituents of the highly filled industrial formulation [65–67, 75, 76].

In the full-range XRD patterns, all samples exhibited a strong and sharp reflection at approximately 26°–27°, together with weaker reflections at higher angles. Since these reflections were also present in the unmodified BMC sample, they were mainly attributed to the graphitic/carbonaceous filler constituents of the BMC formulation rather than to newly formed crystalline phases after MXene addition. This interpretation is consistent with graphite-containing bipolar plate and polymer/graphite composite studies, where the intense reflection around 26°–27° is assigned to graphitic/carbonaceous crystalline structures [67, 68].

The enlarged low-angle region in Figure 7b provides more specific information on the MXene-added composites. The unmodified BMC sample did not show a distinct low-angle reflection in this region. In contrast, the MXene-added composites exhibited a broad MXene-related feature around 6.0°–6.3°, which can be assigned to the low-angle (002) reflection of layered $Ti_3C_2T_x$ MXene. This feature was weak and broad in BMC/MXene-0.24 and BMC/MXene-0.48, but became more

TABLE 5 | FTIR band assignments and the effect of $Ti_3C_2T_x$ MXene incorporation in BMC composites.

Approximate band (cm^{-1})	Band assignment	Origin	Effect of MXene incorporation
3400–3300	O—H stretching	Adsorbed water and residual hydroxyl groups of the BMC matrix and filler phases; additionally the –OH surface terminations of $Ti_3C_2T_x$ MXene in the MXene-added groups	The band broadened with increasing MXene content due to enhanced hydrogen-bonding interactions between MXene surface terminations and the polymer matrix.
2920–2850	C—H stretching	Unsaturated polyester/ styrene matrix	The peak position remains nearly unchanged, while the intensity may slightly decrease because of the filler effect.
1730–1715	C═O stretching	Unsaturated polyester resin	A slight shift toward lower wavenumbers and band broadening were observed, indicating interfacial interactions between the ester groups and MXene surface functionalities.
1635–1600	Aromatic C═C stretching	Styrene aromatic ring and absorbed water	The band may become slightly broader owing to the hydroxyl-terminated surface of $Ti_3C_2T_x$ MXene.
1455–1410	CH_2 bending	Polyester matrix	No significant chemical change is expected; only minor variations in intensity may be observed.
1260–1150	C—O—C stretching	Ester linkage of the polyester matrix	Slight intensity variations may occur due to interfacial interactions between the matrix and MXene.
1120–1030	C—O stretching	Polyester matrix	Minor changes in peak intensity or slight shifts may be observed following MXene incorporation.
760–700	Aromatic C—H out-of-plane bending	Styrene aromatic ring	Generally remains unchanged after MXene addition.
650–550	Ti—O bending vibration	Surface TiO_x on $Ti_3C_2T_x$ MXene	One of the characteristic spectral regions of MXene, the absorption may become more pronounced with increasing MXene loading.
520–450	Ti—C vibrations	$Ti_3C_2T_x$ MXene lattice	The absorption intensity increased with increasing MXene content, supporting the presence of Ti-based MXene-related features in the BMC matrix.

distinguishable in BMC/MXene-0.71. The increased visibility of this low-angle reflection with increasing MXene content supports the presence of MXene-related layered domains in the composites [65, 66, 75, 76].

The broad nature of the low-angle MXene-related reflection is important. It suggests that the MXene contribution was not present as a sharp, highly ordered crystalline phase throughout the whole composite. Instead, the broad reflection is consistent with local layered, overlapped, and partially restacked MXene-related regions. This interpretation is also consistent with the TEM observations in Figure 8. Because the MXene contents were below 1 wt.% and the BMC formulation contained a strong carbonaceous/graphitic background, the MXene-related diffraction contribution was expected to be weak and partially masked in the full-range patterns. Therefore, the XRD results were not interpreted as proof of homogeneous MXene dispersion or complete exfoliation.

The main XRD features and their interpretation are summarized in Table 6 [65–68, 75, 76].

Taken together, the XRD results indicate that the main graphitic/carbonaceous structural features of the BMC formulation were retained after $Ti_3C_2T_x$ MXene addition, while the enlarged low-angle region revealed a weak-to-moderate MXene-related (002) contribution that became more distinguishable with increasing MXene content. These observations provide complementary structural support for the presence of MXene-related layered regions, with FTIR, TEM, and SEM–EDS offering additional spectroscopic, morphological, and elemental evidence.

3.6 | TEM Analysis

TEM analysis was performed to obtain local morphological information on the layered regions observed in the $Ti_3C_2T_x$

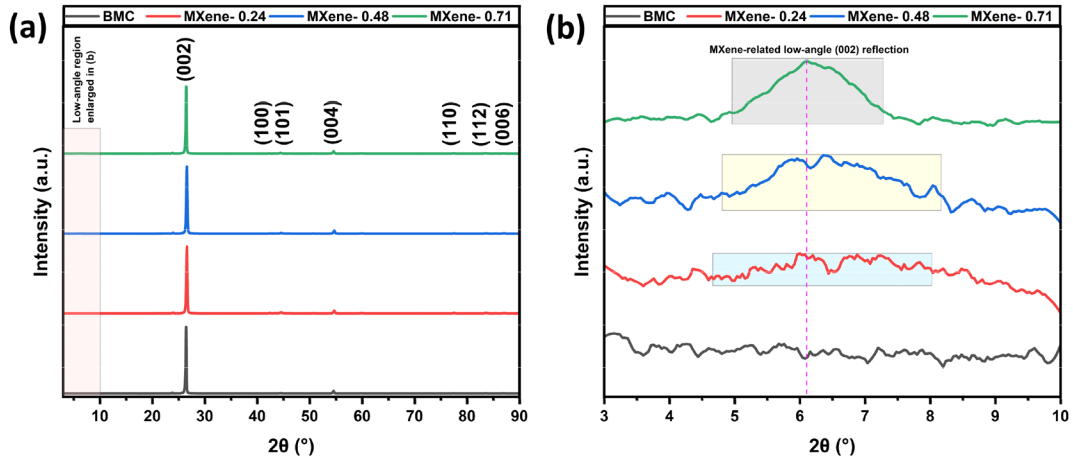

FIGURE 7 | XRD patterns of BMC and $Ti_3C_2T_x$ MXene-added BMC composites: (a) full range from 3° to 90° and (b) enlarged low-angle region from 3° to 10°.

MXene-added BMC composites. Representative TEM micrographs of BMC/MXene-0.24, BMC/MXene-0.48, and BMC/MXene-0.71 are presented in Figure 8. Since $Ti_3C_2T_x$ MXene is known to exhibit a two-dimensional, multilayered, sheet-like morphology with a tendency for intersheet overlap or restacking depending on processing and concentration, the observed lamellar and fringe-like regions were interpreted as MXene-related local layered features. However, because the industrial BMC formulation contains carbonaceous constituents and TEM provides local-area information, the TEM images were not used as standalone proof of homogeneous MXene dispersion or direct chemical identification of every observed layered region [18, 37, 38].

For the BMC/MXene-0.24 sample, the TEM images showed locally observed sheet-like lamellar regions at lower magnification, as shown in Figure 8a. At higher magnifications, parallel layered/fringe-like contrast and localized nanoscale layered texture were observed, as shown in Figure 8b,c. These features are consistent with thin and relatively discrete MXene-related lamellar regions within the examined areas. At this lowest investigated MXene content, dense local accumulation or extensive restacking was not clearly observed. Therefore, the BMC/MXene-0.24 morphology was interpreted as a low-content state in which MXene-related layered features were locally visible but remained comparatively less compact and less overlapped than in the higher-content groups.

For the BMC/MXene-0.48 sample, elongated sheet-like lamellar regions and partially overlapped lamellar areas were observed, as shown in Figure 8d. The higher-magnification images revealed possible partially restacked edges, parallel fringe-like layered domains, and localized nanoscale stacked texture, as shown in Figure 8e,f. Compared with BMC/MXene-0.24, the lamellar features in BMC/MXene-0.48 appeared more integrated and more visibly overlapped within the selected local regions. This observation suggests a concentration-dependent increase in local contact and partial overlap of MXene-related lamellar structures when the MXene content increased from 0.24 to 0.48 wt.%. This interpretation is consistent with the mechanical results, where BMC/MXene-0.48 showed improved tensile strength, impact energy, and hardness together with comparatively repeatable mechanical behavior.

For the BMC/MXene-0.71 sample, large overlapped sheet-like regions and locally dense overlapped regions were more evident at lower magnification, as shown in Figure 8g. The intermediate- and higher-magnification images showed thickened overlap regions, possible local restacking, parallel fringe-like domains, and dense nanoscale layered texture, as shown in Figure 8h,i. At 0.71 wt.% MXene, the layered regions appeared denser and more compact than those observed in the lower-content samples. This morphology coincided with the greater mean tensile strength, impact energy, and Shore D hardness measured for BMC/MXene-0.71. At the same time, the presence of locally dense or thickened regions suggests that increasing MXene content may also increase the tendency for local restacking or accumulation, which is consistent with the higher scatter observed in some mechanical results for this group.

Therefore, the TEM observations support a concentration-dependent transition from relatively discrete lamellar features at 0.24 wt.% MXene to partially overlapped regions at 0.48 wt.% and more locally dense/restacked layered regions at 0.71 wt.% MXene. The corresponding SEM–EDS results further supported the presence of Ti-containing MXene-related regions. The inference remains limited to the areas actually examined [18, 43, 47]. The TEM observations complement the SEM–EDS findings by showing local layered/fringe-like MXene-related morphologies, while SEM–EDS provides elemental support for Ti-containing regions over selected powder and bulk observation areas.

3.7 | SEM–EDS-Based Microstructural Interpretation

Scanning electron microscopy combined with energy-dispersive X-ray spectroscopy (SEM–EDS) was used to examine the morphological features of the powder mixtures and compression-molded bulk composites and to identify Ti-containing MXene-related regions. Because the industrial BMC system already contains heterogeneous carbonaceous and filler-rich

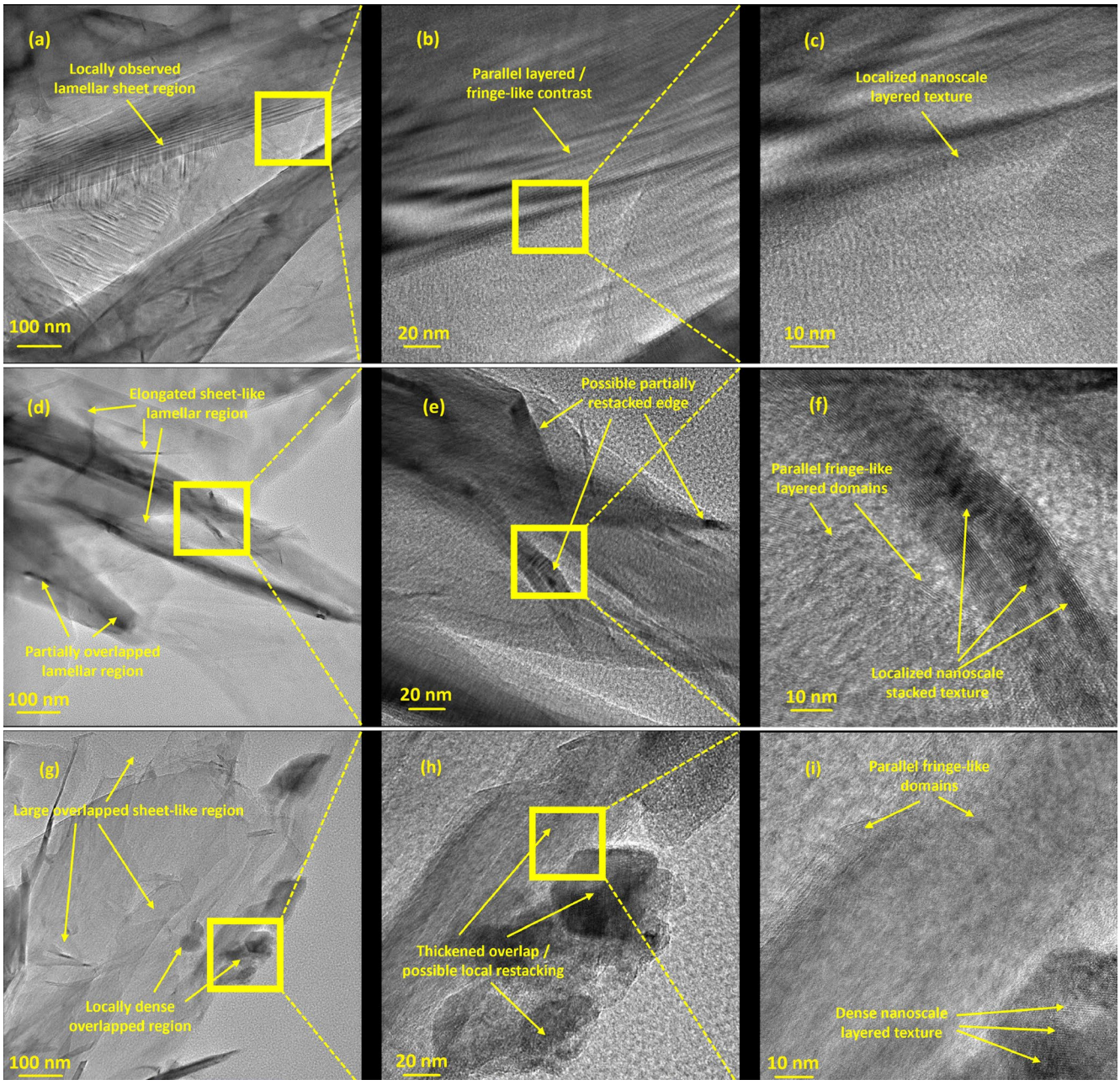

FIGURE 8 | TEM micrographs of (a–c) BMC/MXene-0.24, (d–f) BMC/MXene-0.48, and (g–i) BMC/MXene-0.71 at increasing magnifications. Boxes indicate the regions examined at higher magnification.

constituents, SEM observations alone were not considered sufficient to distinguish MXene-related structures from the BMC background. Therefore, SEM images were interpreted together with the corresponding EDS maps and spectra. In this study, the SEM–EDS results were used as complementary microstructural evidence and were not treated as standalone proof of homogeneous MXene dispersion or direct interfacial strengthening [18, 48].

The powder-state SEM images and corresponding SEM–EDS results are presented in Figure 9. The unmodified BMC powder mixture exhibited irregular, plate-like, and heterogeneous particles, which is consistent with the complex multi-component nature of the BMC formulation. In the EDS spectrum of the unmodified BMC powder mixture, carbon was the dominant detected element, and no Ti signal was observed. This observation is important because it indicates that Ti-containing signals detected in the MXene-added groups can be associated with $Ti_3C_2T_x$ MXene-related regions rather than with the original BMC formulation [37, 38].

After $Ti_3C_2T_x$ MXene addition, weak but detectable Ti signals appeared in the EDS spectra of the powder mixtures. The Ti content obtained from the mapped regions increased from approximately 0.1 atomic percent (at.%) for BMC/MXene-0.24 to 0.2 at.% for BMC/MXene-0.48 and 0.3 at.% for BMC/MXene-0.71. This trend is consistent with the increasing amount of MXene added to the BMC powder mixture. In the corresponding SEM images and EDS maps, Ti-marked regions were observed on or between the carbonaceous and filler-rich particles. For BMC/

TABLE 6 | Main XRD features observed in unmodified BMC and $Ti_3C_2T_x$ MXene-added BMC composites.

Approximate 2θ region (°)	Assigned feature	Main observation in this study	Interpretation	References
6.0–6.3	$Ti_3C_2T_x$ MXene-related low-angle (002) reflection	Not clearly observed in unmodified BMC; weak/broad in BMC/MXene-0.24 and BMC/MXene-0.48; more distinguishable in BMC/MXene-0.71	Supports the presence of MXene-related layered/restacked domains within the low-content BMC/MXene composites	[65, 66, 75, 76]
26–27	Graphitic/carbonaceous (002) reflection	Strong and sharp reflection observed in all samples, including unmodified BMC	Mainly attributed to the conductive carbonaceous/graphitic constituents of the BMC formulation rather than to MXene addition	[67, 68]
43–45	Graphitic/carbonaceous-related reflections	Weak reflections observed in all samples	Associated with carbonaceous/graphitic components already present in the BMC system	[67, 68]
54–56	Carbonaceous/graphitic high-angle reflection	Weak reflections observed in all samples	Indicates retention of the carbonaceous crystalline contribution of the BMC formulation	[67, 68]
77–84	Carbonaceous/graphitic high-angle reflections	Weak high-angle reflections were observed in all samples	Related to the graphitic/carbonaceous filler background of the BMC formulation	[67, 68]

MXene-0.24, the Ti signal appeared limited and localized. For BMC/MXene-0.48, Ti-containing regions appeared more visible over the mapped area, suggesting a more widespread distribution tendency within the powder mixture. For BMC/MXene-0.71, the Ti signal intensity increased further; however, several local Ti-rich regions were also apparent. These powder-state observations support the presence of Ti-containing MXene-related regions before compression molding, within the limits of the mapped areas [18, 43, 52].

The SEM images and corresponding SEM–EDS results of the compression-molded bulk composites are presented in Figure 10. The unmodified BMC bulk specimen exhibited a compact and heterogeneous morphology typical of a compression-molded, highly filled thermoset composite. Similar to the powder-state results, no Ti signal was detected in the EDS spectrum of the unmodified bulk BMC specimen. In contrast, Ti signals were detected in all MXene-added bulk composites, again supporting the presence of Ti-containing MXene-related regions after compression molding.

In the bulk composites, the Ti content obtained from the mapped areas was approximately 0.1 at.% for BMC/MXene-0.24, 0.2 at.% for BMC/MXene-0.48, and 0.3 at.% for BMC/MXene-0.71. The BMC/MXene-0.24 specimen showed a limited number of Ti-containing regions distributed over the mapped area. The BMC/MXene-0.48 specimen exhibited a more visible and relatively more widespread Ti signal distribution within the observed region. By contrast, the BMC/MXene-0.71 specimen showed stronger Ti-rich zones, but these regions also appeared more localized in certain areas. This behavior suggests that increasing MXene content increased the detectability of Ti-containing regions, while the highest addition level also showed a tendency toward more locally concentrated Ti-rich areas [18, 49].

The combined powder-state and bulk SEM–EDS observations indicate that Ti-containing MXene-related regions were present both before and after compression molding. At the same time, the results also show the limitations of the method. SEM images alone do not allow direct distinction of MXene from the heterogeneous carbon-rich BMC background, and EDS mapping at the present scale does not prove homogeneous nanoscale dispersion. Therefore, the SEM–EDS results were used primarily to identify Ti-containing regions and compare distribution tendencies among the groups.

BMC/MXene-0.48 showed lower scatter in tensile strength and impact energy, and its Ti signal covered a broader part of the mapped area. BMC/MXene-0.71 had higher mean mechanical values, but the Ti-rich regions were more localized. This interpretation is consistent with the increased specimen-to-specimen variation observed in some of the mechanical data. Accordingly, the SEM–EDS results support the view that low-content $Ti_3C_2T_x$ MXene addition can contribute to the performance of industrial BMC composites, while the highest investigated addition level may also increase the tendency for local accumulation or agglomeration-related features. For this reason, the SEM–EDS findings were interpreted as supportive microstructural evidence [39, 48].

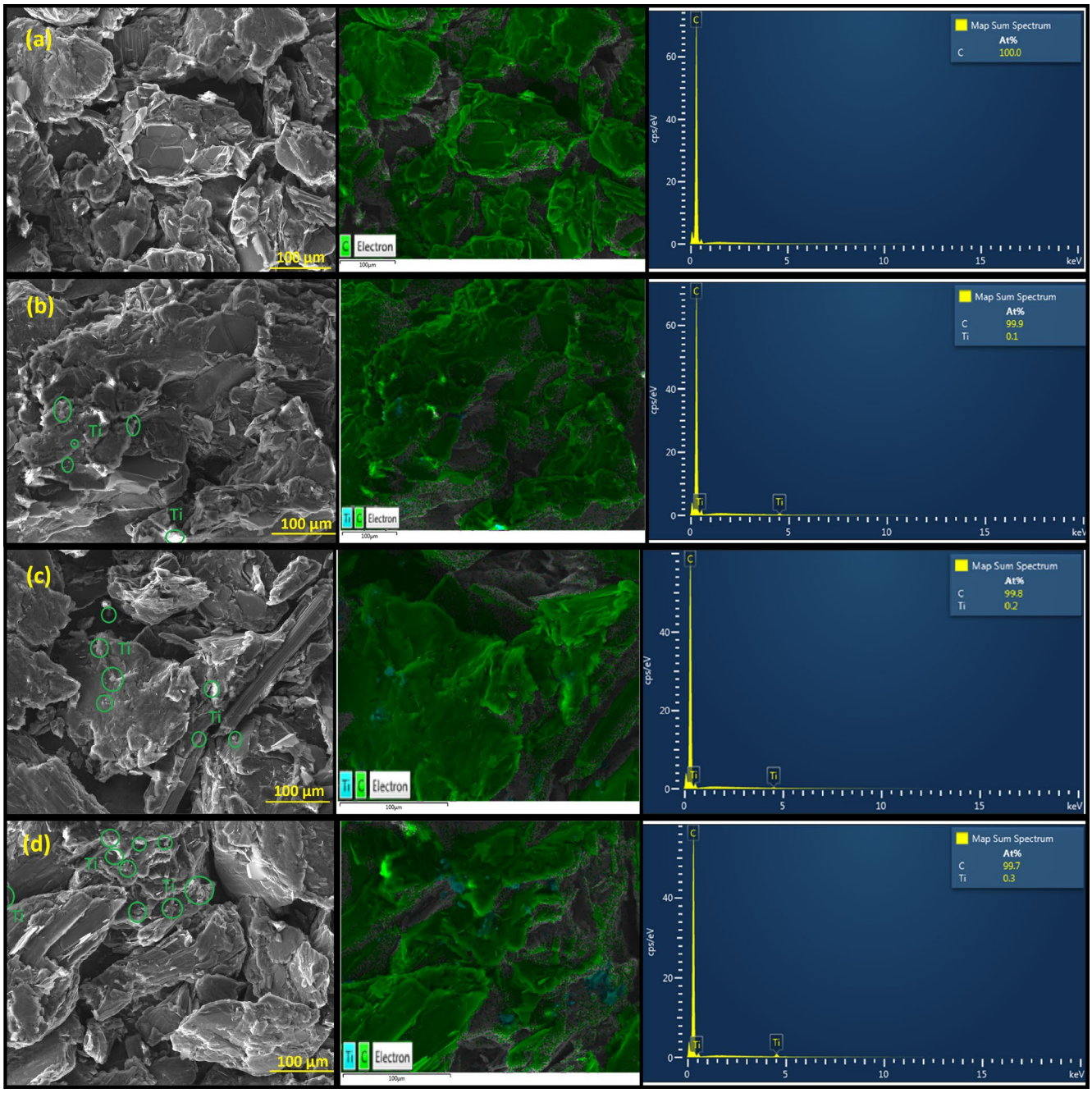

FIGURE 9 | Powder-state SEM images, elemental maps, and EDS spectra of (a) BMC, (b) BMC/MXene-0.24, (c) BMC/MXene-0.48, and (d) BMC/MXene-0.71.

The SEM–EDS observations also complement the TEM findings. TEM provided local visual evidence of layered/fringe-like MXene-related regions, while SEM–EDS provided elemental support for Ti-containing regions over selected powder and bulk observation areas. Therefore, TEM and SEM–EDS were interpreted together to discuss the local distribution tendency of MXene-related regions rather than to claim whole-sample homogeneous dispersion.

3.8 | Structure–Property Relationship

The mechanical performance of the $Ti_3C_2T_x$ MXene-added BMC composites should be interpreted together with the complementary spectroscopic, structural, and microstructural observations. The tensile, impact, and Shore D hardness results showed that low-content MXene addition improved the mechanical response of the industrial BMC system. However, these improvements should not be assigned to a single mechanism based only on mechanical testing. Instead, the observed behavior should be considered as the combined result of MXene-related regions, local matrix–filler contact, filler-rich BMC morphology, and the heterogeneous nature of the compression-molded thermoset composite [18].

To place the mechanical improvements observed in the present BMC/MXene system into a broader context, representative quantitative results from open literature on BMC systems, MXene/

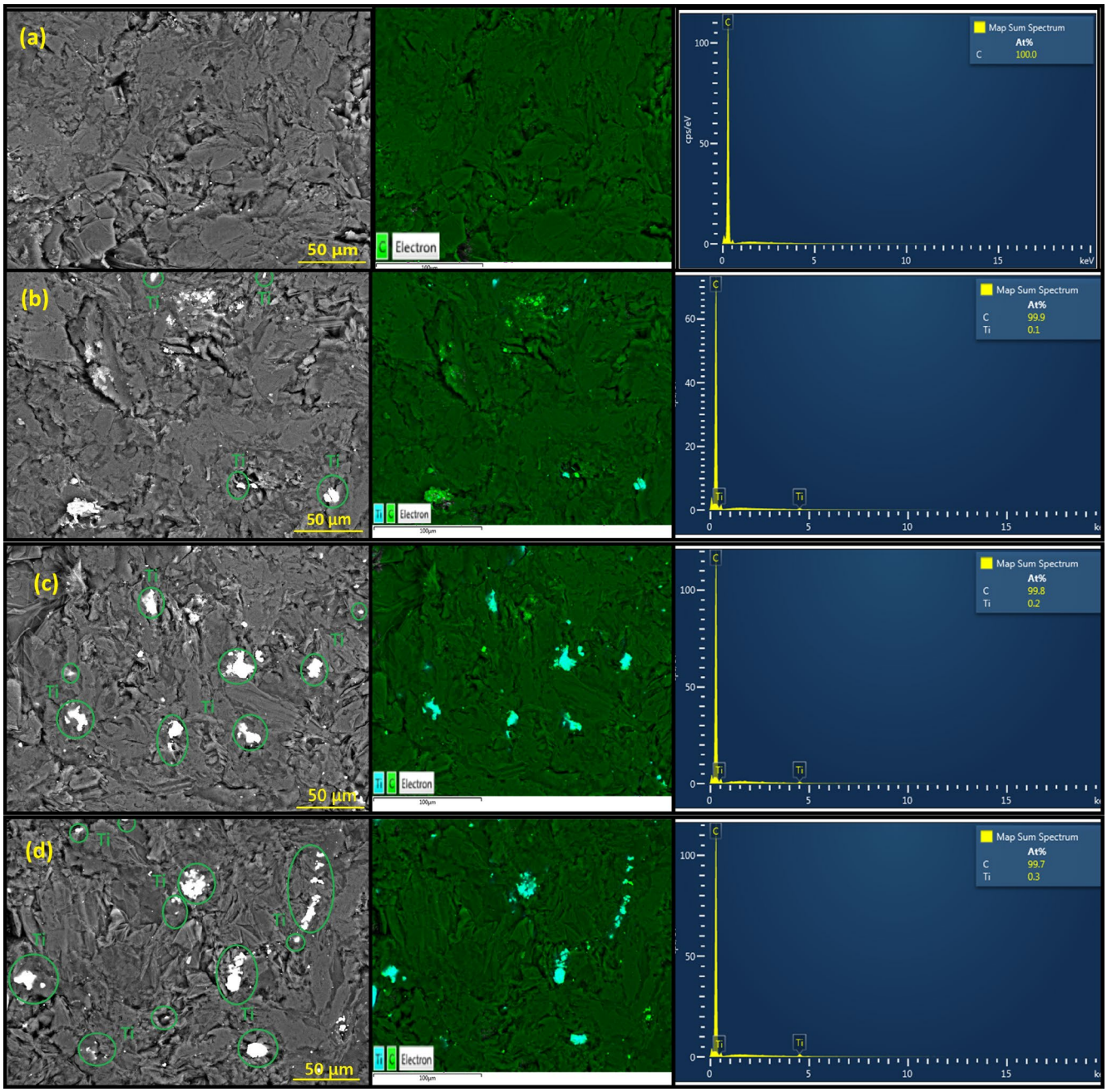

FIGURE 10 | SEM images, elemental maps, and EDS spectra of compression-molded bulk composites: (a) BMC, (b) BMC/MXene-0.24, (c) BMC/MXene-0.48, and (d) BMC/MXene-0.71.

polymer composites, and related two-dimensional filler/polymer composites are summarized in Table 7. The comparison is not intended to provide a direct one-to-one equivalence because the matrices, filler types, processing routes, filler contents, and testing modes differ among the studies. Instead, the table is used to show how low-content $Ti_3C_2T_x$ MXene addition in the present highly filled industrial BMC system compares with reported property changes in related composite systems.

The first row of Table 7 summarizes the results of the present study, while the remaining rows list reported values for BMC, MXene/polymer, and related two-dimensional filler/polymer composite systems. The magnitude of mechanical improvement in these systems depends strongly on the matrix type, filler loading, filler distribution state, surface chemistry, processing route, and testing method. The present work differs from most of the listed studies in that $Ti_3C_2T_x$ MXene was added at below 1 wt.% into an already highly filled industrial BMC formulation and processed by compression molding without changing the established molding route. The values given in the first row should therefore not be compared in absolute terms with neat epoxy, PVA, Elium, coating, or hybrid nanocomposite systems, whose unfilled or lightly filled matrices provide a considerably lower mechanical baseline. Read against this difference in baseline, the comparison indicates that the improvements obtained in the present study are meaningful within the context of a highly filled BMC system, in which the initial stiffness, solid content, and processing constraints are already significant.

TABLE 7 | Quantitative comparison of mechanical property changes reported for BMC, MXene/polymer, and related two-dimensional filler/polymer composites.

Composite system/study focus	Added filler/modification and loading	Evaluated property	Reported result/change	References
Present study—industrial highly filled BMC composite	0.714 wt.% $Ti_3C_2T_x$ MXene; compression molded under unchanged industrial molding conditions	Tensile strength, tensile modulus, Izod impact energy, Shore D hardness	Tensile strength increased by 68.6% (14.24 → 24.00 MPa); tensile modulus increased by 29.1% (7.85 → 10.14 GPa); absorbed impact energy increased by 52.6%; Shore D hardness increased by 7.4%, all relative to unmodified BMC.	—
Jute chopped fiber reinforced BMC	Calcium carbonate or kaolin filler in jute chopped fiber BMC	Tensile strength and Young's modulus	Calcium carbonate-filled BMC showed reported tensile strength and Young's modulus values of approximately 21 MPa and 9.6 GPa; large scatter was reported for BMC specimens.	[2]
Short glass fiber compression-molded BMC	Fiber shortening by extended mixing in $CaCO_3$-filled BMC	Charpy impact strength	Average Charpy impact value increased by approximately 26.1%, from 7.63 to 9.62 kJ m^{-2}.	[13]
Injection-molded glass fiber reinforced BMC	Sub-millimeter fiber spacing/ shortened glass fiber configuration	Tensile modulus	Initial and maximum tensile modulus increased by approximately 5%–25%, depending on fiber-spacing-related microstructural conditions.	[14]
Glass fiber reinforced BMC	E-glass fiber length shortened from 6.4 mm to 0.44 mm in BMC containing 20 mass% E-glass fiber	Tensile strain and tensile strength	Fracture strain increased by almost 40%, and tensile strength increased by almost 60% compared with longer-fiber BMC-GFRP samples.	[15]
MXene/epoxy nanocomposite interface study	MXene loading up to and above 1 vol.%	Young's modulus and interface-related mechanical response	Young's modulus increased up to a certain MXene content, while the effectiveness was reduced at higher contents because of the tendency for filler aggregation.	[39]
Ti_3CN MXene/epoxy composite	High Ti_3CN MXene loading, up to 90 wt.%	Young's modulus and creep resistance	Young's modulus reached 12.8 GPa at high MXene loading; creep resistance increased by 46% compared with neat epoxy.	[40]

(Continues)

TABLE 7 | (Continued)

Composite system/study focus	Added filler/modification and loading	Evaluated property	Reported result/change	References
$Ti_3C_2T_x$ MXene/MWCNT epoxy nanocomposite	1 wt.% MWCNT–MXene hybrid filler	Young's modulus, flexural modulus, and fracture toughness	Young's modulus and flexural modulus increased by 31% and 28%, respectively; fracture toughness increased by 84.5% compared with neat epoxy.	[41]
$Ti_3C_2T_x$ MXene/Elium composite	0.75 wt.% $Ti_3C_2T_x$ MXene	Tensile strength, flexural strength, fracture toughness	Tensile strength reached 69.45 MPa, flexural strength reached 110 MPa, and fracture toughness increased by 31% compared with neat Elium.	[52]
$Ti_3C_2T_x$ MXene/PVA nanocomposite	0.6 wt.% $Ti_3C_2T_x$ MXene	Young's modulus and tensile strength	Young's modulus increased by 27%, and tensile strength improved by 24%.	[54]
$Ti_3C_2T_x$ MXene/MoS_2 hybrid epoxy coating	0.5 wt.% MXene/MoS_2 hybrid nanofiller	Tensile strength, hardness, and storage modulus	Tensile strength increased by approximately 3.5 times; hardness increased by 112% from 146.6 to 311.4 MPa; storage modulus increased by 45% from 1354 to 1958 MPa.	[55]
MXene-functionalized short carbon fiber/epoxy composite	$Ti_3C_2T_x$-functionalized short carbon fibers	Tensile strength and flexural strength	Tensile strength increased from 124.6 to 141.2 MPa, while flexural strength increased from 165.7 to 199.3 MPa.	[57]
Low-content $Ti_3C_2T_x$ MXene/epoxy composite	0.1 wt.% multilayer or few-layer $Ti_3C_2T_x$ MXene	Tensile strength retention after hydrothermal aging	After 400 h of hydrothermal aging, tensile strength retention was 85.3% for multilayer MXene/epoxy and 83.0% for few-layer MXene/epoxy, compared with 69.1% for neat epoxy.	[60]
$Ti_3C_2T_x$ MXene/epoxy composite	0.2 wt.% $Ti_3C_2T_x$ MXene	Tensile strength and flexural strength	Tensile strength increased by 51%, and flexural strength increased by 32%.	[77]
PEI-functionalized $Ti_3C_2T_x$ MXene/epoxy composite	0.5 wt.% PEI-functionalized $Ti_3C_2T_x$ MXene	Compressive strength and fracture toughness	Compressive strength increased by approximately 40%; KIC and GIC increased by approximately 70% and 140%, respectively. At higher loading, agglomeration reduced the mechanical benefit.	[78]

(Continues)

TABLE 7 | (Continued)

Composite system/study focus	Added filler/modification and loading	Evaluated property	Reported result/change	References
Ti_3C_2 MXene-functionalized carbon fiber/epoxy composite	Ti_3C_2 MXene functionalization on carbon fiber surface	Wettability and interfacial shear strength	MXene functionalization improved the wettability of the carbon fiber surface and increased the interfacial shear strength by 186% compared with nonfunctionalized specimens.	[79]
$Ti_3C_2T_x$ MXene/MWCNT/PVA ternary nanocomposite	1.2 wt.% $Ti_3C_2T_x$/f-CNT hybrid filler	Young's modulus and tensile strength	Young's modulus and tensile strength improved by approximately 52% and 48%, respectively, compared with pure PVA.	[80]
Surface-functionalized $Ti_3C_2T_x$ MXene/epoxy nanocomposite	0.12 vol.% surface-functionalized $Ti_3C_2T_x$ MXene	Mechanical strength and multifunctional properties	Surface functionalization improved compatibility with the epoxy matrix and mechanical strength improvements exceeding 100% were reported at low filler loading.	[81]

The literature comparison also supports the cautious interpretation adopted in this study. Previous BMC studies have shown that fiber length, filler type, filler configuration, and processing-related microstructural features can markedly influence tensile strength, tensile modulus, impact behavior, and data scatter in molded thermoset composites [2, 13–15]. Similarly, MXene/polymer studies have reported that $Ti_3C_2T_x$ MXene can improve tensile, flexural, compressive, fracture-related, interfacial, hardness, and durability-related properties at low or moderate contents when the filler morphology, surface state, and matrix compatibility are favorable [39–41, 52, 54, 55, 57, 60, 77, 80]. At the same time, several studies emphasize that excessive filler loading, local aggregation, nanosheet restacking, and insufficient distribution can reduce the effectiveness of MXene addition or increase variability in mechanical response [18, 39, 43–45, 47]. These literature findings are consistent with the present results, where increasing MXene content improved the average mechanical response, while the highest MXene content also showed greater scatter in some mechanical properties.

The FTIR results indicated that the main spectral features of the BMC system were largely preserved after $Ti_3C_2T_x$ MXene addition. Slight broadening or intensity variations in the O—H, C═O, C—O—C, and C—O related regions may be associated with local interactions between the polyester/styrene-based matrix and MXene surface terminations. In addition, the low-wavenumber Ti—O and Ti—C related contributions became more distinguishable with increasing MXene content, supporting the identification of Ti-containing MXene-related spectral features. These observations suggest that the mechanical improvements were not mainly associated with a dominant chemical transformation of the BMC matrix. Rather, the FTIR results support a predominantly physical contribution of low-content MXene addition, including local matrix–filler contact and hydrogen-bonding-type interaction tendencies [18, 26, 37–39, 48].

The XRD results complemented the FTIR, TEM, and SEM–EDS findings by separating the dominant carbonaceous/graphitic background of the BMC formulation from the weak MXene-related low-angle contribution. The full-range XRD patterns were dominated by graphitic/carbonaceous reflections that were already present in the unmodified BMC sample, indicating that low-content MXene addition did not produce a major detectable high-angle crystalline phase change in the BMC structure. In contrast, the enlarged low-angle region showed a broad MXene-related (002) reflection around 6.0°–6.3°, which became more distinguishable with increasing MXene content. The broad low-angle reflection was assigned to MXene-related layered domains; however, its weak intensity and broad profile do not establish homogeneous dispersion or complete exfoliation. This interpretation is consistent with TEM observations, where the MXene-added composites showed local layered, overlapped, and partially restacked regions rather than uniform nanoscale dispersion throughout the whole BMC structure [65–68, 75, 76].

TEM observations provided local morphological evidence of layered, fringe-like, overlapped, and locally stacked MXene-related regions in the MXene-added composites. The BMC/MXene-0.24 sample showed relatively discrete local lamellar features, whereas BMC/MXene-0.48 showed more visible partial overlap and BMC/MXene-0.71 showed more locally dense

or restacked layered regions. These observations support a concentration-dependent change in local MXene-related morphology [18, 43, 47].

The SEM–EDS results further supported the presence of Ti-containing MXene-related regions in both the powder mixtures and the compression-molded bulk composites. The unmodified BMC showed no Ti signal, whereas Ti signals were detected in all MXene-added groups. The Ti signal became more detectable with increasing MXene content, which is consistent with the increasing addition amount. The Ti signal covered a wider part of the mapped area in BMC/MXene-0.48, whereas stronger signals were confined to smaller regions in BMC/MXene-0.71. This distinction is important for interpreting the mechanical results: BMC/MXene-0.71 led all groups in mean tensile strength, tensile modulus, impact energy, and Shore D hardness, while BMC/MXene-0.48 showed more repeatable mechanical behavior in several measurements [16, 18, 21].

The different mechanical tests also reflect different aspects of the structure–property relationship. Tensile strength is related to the maximum stress-bearing response under quasi-static loading, tensile modulus represents the initial stiffness response, Izod impact energy reflects the energy absorbed during rapid fracture, and Shore D hardness represents localized surface indentation resistance. Therefore, these properties should not be explained by the same mechanism [61, 63, 64]. The stronger increase in tensile strength compared with tensile modulus and Shore D hardness indicates that MXene addition affected ultimate load-bearing behavior more strongly than the initial stiffness or local surface indentation response. Similarly, the limited additional increase in impact energy from BMC/MXene-0.48 to BMC/MXene-0.71 suggests that the fracture-related energy absorption response may begin to level off as the MXene content approaches 0.714 wt.% [18, 43–45].

This relationship suggests that the mechanical response of the BMC/MXene composites was governed not only by the amount of MXene added, but also by the local distribution tendency of Ti-containing MXene-related regions. Increasing MXene content enhanced the average mechanical response, particularly in tensile strength and hardness. However, the higher standard deviation observed in some results for BMC/MXene-0.71 indicates that local heterogeneity may become more relevant at the highest investigated content. At 0.71 wt.%, the mean mechanical values were higher; at 0.48 wt.%, the tensile strength and impact energy data were less scattered, and the Ti signal appeared over a broader area.

Taken together, the results show that low-content $Ti_3C_2T_x$ MXene addition improved the mechanical response of the industrial BMC composites. The improvement was supported by the detection of Ti-containing MXene-related regions, local layered/fringe-like TEM features, and functional group-related spectroscopic contributions. Nevertheless, the present results do not allow the mechanical behavior to be attributed solely to homogeneous MXene dispersion, direct chemical bonding, or a single reinforcement mechanism. For this reason, the structure–property relationship was interpreted as a combined effect of low-content MXene addition, local Ti-containing regions, MXene-related local layered morphology, the highly filled BMC background, and compression-molded bulk microstructure.

4 | Conclusions

In this study, $Ti_3C_2T_x$ MXene was added to an industrial BMC formulation at 0.238, 0.476, and 0.714 wt.%; all groups were prepared using the same mixing and compression-molding parameters.

Average tensile strength rose from 14.24 ± 1.06 MPa in the unmodified BMC to 17.98 ± 0.93, 20.83 ± 0.62, and 24.00 ± 1.88 MPa as the MXene content increased. These values represent gains of 26.3%, 46.3%, and 68.6%. Tensile modulus changed from 7.85 ± 0.35 GPa to 8.47 ± 0.67, 9.58 ± 0.75, and 10.14 ± 1.05 GPa, equivalent to increases of 7.9%, 22.0%, and 29.1%. The smaller modulus gains show that the initial stiffness response changed less than the tensile strength.

Absorbed impact energy increased by 27.4%, 46.0%, and 52.6%, reaching 0.066 ± 0.004 J in BMC/MXene-0.71. Shore D hardness rose by 2.5%, 5.1%, and 7.4%, reaching 75.8 ± 0.84 in the same group. The hardness change was therefore more limited than the tensile and impact improvements.

The main BMC bands were largely retained in the FTIR spectra. Slight changes occurred in the O—H, C═O, C—O—C, and C—O regions, while the low-wavenumber Ti—O and Ti—C contributions became more distinguishable as the MXene content increased.

The XRD patterns were dominated by the graphitic/carbonaceous background of the BMC formulation. A broad MXene-related (002) feature at approximately 6.0°–6.3° became clearer with increasing MXene content and was assigned to layered MXene-related domains. Its weak and broad profile was not taken as evidence of homogeneous dispersion or complete exfoliation.

TEM images contained lamellar, fringe-like, overlapping, and locally restacked features within the selected areas. Thicker and denser regions were more evident at 0.714 wt.% MXene.

SEM–EDS detected Ti in all MXene-added powder mixtures and bulk composites, whereas no Ti signal was found in unmodified BMC. Within the mapped areas, BMC/MXene-0.48 displayed a broader Ti distribution, while BMC/MXene-0.71 contained stronger but more localized signals.

The results demonstrate that low-content $Ti_3C_2T_x$ MXene addition can improve the mechanical response of industrial BMC composites under unchanged compression-molding conditions. The observed improvements were interpreted in terms of the combined effects of MXene addition, Ti-containing MXene-related regions, local matrix–filler contact, local layered morphology, and the highly filled BMC microstructure. None of the characterization results presented here establishes homogeneous MXene dispersion, direct chemical bonding, or a single confirmed reinforcement mechanism, and the interpretation is therefore kept at the level supported by the data. Future work

involving broader processing windows, higher-resolution local chemical analysis, and larger-area statistical imaging may provide deeper insight into the relationship between MXene distribution, local accumulation, and mechanical response.

Author Contributions

Bilge Yılmaz: conceptualization, methodology, investigation, writing – original draft, writing – review and editing, visualization, data curation, supervision, resources. **Cemal Meran:** validation, supervision, resources, writing – review and editing. **Cahit Bilgi:** conceptualization, investigation, resources, writing – review and editing, visualization.

Acknowledgments

The authors would like to acknowledge Debak for their support in BMC material supply, industrial processing conditions, and composite plate production. The authors also thank Pamukkale University for supporting the mechanical characterization studies, including tensile and impact testing. The authors gratefully acknowledge Istanbul University-Cerrahpaşa, Advanced Composite Laboratory, for their support in Shore D hardness measurements and FTIR analysis. The SEM–EDS and XRD analyses were carried out with the support of Bartın University Central Research Laboratory Application and Research Center (BÜMLAB), and the authors gratefully acknowledge the laboratory staff for their technical assistance during microstructural and structural characterization. The authors also acknowledge Bayburt University Central Research Laboratory Application and Research Center (BUMER) for their support in TEM analysis.

Funding

The authors have nothing to report.

Consent

Contributions from each of the authors of this article are acknowledged. This article has not been published or uploaded anywhere before. The authors of this article are aware that the article is uploaded and published in this journal.

Conflicts of Interest

The authors declare no conflicts of interest.

Data Availability Statement

The data supporting the findings of this study are included within the article. Additional information related to the experimental data may be made available by the corresponding author upon reasonable request.

References

1. T. Hsieh, T. Chang, C. Chen, and S. Tsai, "The Effect of Aging on the Mechanical Properties of Bulk Molding Compound With Different Fiber Lengths," *Polymer Composites* 46 (2025): 1714–1724, https://doi.org/10.1002/pc.29067.

2. M. I. Lautenschläger, L. Mayer, J. Gebauer, K. A. Weidenmann, F. Henning, and P. Elsner, "Comparison of Filler-Dependent Mechanical Properties of Jute Fiber Reinforced Sheet and Bulk Molding Compound," *Composite Structures* 203 (2018): 960–967, https://doi.org/10.1016/j.compstruct.2017.09.100.

3. S. Sreenivasan, S. Sulaiman, B. T. H. T. Baharudin, M. K. A. Ariffin, and K. Abdan, "Mechanical Properties of Novel Kenaf Short Fiber Reinforced Bulk Molding Compounds (BMC)," *Advances in Materials and Processing Technologies* 1 (2015): 49–55, https://doi.org/10.1080/2374068X.2015.1112130.

4. R. d. A. Aragão, I. T. Azevedo, and K. Soares, "Process-Property Relationships of Sheet Molding Compound Composites With Calcium Carbonate and Hollow-Glass Microsphere Loadings," *Materials Science and Technology* (2025), https://doi.org/10.1177/02670836251340121.

5. V. Austermann, J. Neuhaus, D. Schneider, R. Dahlmann, and C. Hopmann, "Investigation of the Mechanical Properties of Vinylester-Based Sheet Moulding Compound (SMC) Subject to Particle Recycling," *Journal of Composites Science* 6 (2022): 84, https://doi.org/10.3390/jcs6030084.

6. M. E. Arı, C. Bilgi, and B. Demir, "Composite Materials in Railway Vehicles: Performance and Application Perspectives—A Review," *Arabian Journal for Science and Engineering* (2026), https://doi.org/10.1007/s13369-026-11354-3.

7. O. A. Alo, I. O. Otunniyi, and E. R. Sadiku, "Processing Methods for Conductive Polymer Composite Bipolar Plates: Effect on Plate Quality and Performance," *Fuel Cells* 23 (2023): 136–160, https://doi.org/10.1002/fuce.202100157.

8. S. Simaafrookhteh, M. Khorshidian, and M. Momenifar, "Fabrication of Multi-Filler Thermoset-Based Composite Bipolar Plates for PEMFCs Applications: Molding Defects and Properties Characterizations," *International Journal of Hydrogen Energy* 45 (2020): 14119–14132, https://doi.org/10.1016/j.ijhydene.2020.03.105.

9. M.-C. Hsiao, S.-H. Liao, M.-Y. Yen, et al., "Effect of Graphite Sizes and Carbon Nanotubes Content on Flowability of Bulk-Molding Compound and Formability of the Composite Bipolar Plate for Fuel Cell," *Journal of Power Sources* 195 (2010): 5645–5650, https://doi.org/10.1016/j.jpowsour.2010.03.065.

10. S. H. Lee, S. M. Lee, S. Park, D.-H. Jung, W.-J. Song, and Y.-S. Lee, "Enhanced Mechanical and Electrical Properties of Carbon Composite Bipolar Plates in PEMFCs via Wet Mixing and CNT Optimization," *Advances in Industrial and Engineering Chemistry* 1 (2025): 27, https://doi.org/10.1007/s44405-025-00020-1.

11. A. Gomez-Sanchez, V. A. Franco-Luján, H. M. Alfaro-López, L. Hernández-Sánchez, H. Cruz-Martínez, and D. I. Medina, "Carbon Material-Reinforced Polymer Composites for Bipolar Plates in Polymer Electrolyte Membrane Fuel Cells," *Polymers* 16 (2024): 671, https://doi.org/10.3390/polym16050671.

12. H. M. Irshad and S. Shahgaldi, "Comprehensive Review of Bipolar Plates for Proton Exchange Membrane Fuel Cells With a Focus on Materials, Processing Methods and Characteristics," *International Journal of Hydrogen Energy* 111 (2025): 462–487, https://doi.org/10.1016/j.ijhydene.2025.02.300.

13. M. C. Faudree, Y. Nishi, and M. Salvia, "Increasing Impact Strength of a Short Glass Fiber Compression Molded BMC by Shortening Fibers Without Change in Equipment," *Materials* 15 (2022): 1145, https://doi.org/10.3390/ma15031145.

14. M. C. Faudree, Y. Nishi, and M. Gruskiewicz, "A Novel 'Fiber-Spacing' Model of Tensile Modulus Enhancement by Shortening Fibers to Sub-Millimeter in an Injection-Molded Glass Fiber Reinforced Polymer Bulk Molding Compound (GFRP-BMC)," *Materials Transactions* 55 (2014): 1292–1298, https://doi.org/10.2320/matertrans.M2014070.

15. M. C. Faudree and Y. Nishi, "Tensile Strength Enhancement by Shortening Glass Fibers With Sub-Millimeter Length in Bulk Molding Polymer Compound," *Materials Transactions* 51 (2010): 2304–2310, https://doi.org/10.2320/matertrans.M2010121.

16. P. Govindaraj, A. Sokolova, N. Salim, et al., "Distribution States of Graphene in Polymer Nanocomposites: A Review," *Composites Part B: Engineering* 226 (2021): 109353, https://doi.org/10.1016/j.compositesb.2021.109353.

17. U. Kilic, M. M. Sherif, and O. E. Ozbulut, "Tensile Properties of Graphene Nanoplatelets/Epoxy Composites Fabricated by Various Dispersion Techniques," *Polymer Testing* 76 (2019): 181–191, https://doi.org/10.1016/j.polymertesting.2019.03.028.

18. H. Cao, N. N. Neal, S. Pas, et al., "Architecting MXenes in Polymer Composites," *Progress in Polymer Science* 153 (2024): 101830, https://doi.org/10.1016/j.progpolymsci.2024.101830.

19. T. Kuilla, S. Bhadra, D. Yao, N. H. Kim, S. Bose, and J. H. Lee, "Recent Advances in Graphene Based Polymer Composites," *Progress in Polymer Science* 35 (2010): 1350–1375, https://doi.org/10.1016/j.progpolymsci.2010.07.005.

20. J. R. Potts, D. R. Dreyer, C. W. Bielawski, and R. S. Ruoff, "Graphene-Based Polymer Nanocomposites," *Polymer* 52 (2011): 5–25, https://doi.org/10.1016/j.polymer.2010.11.042.

21. K. Bilisik and M. Akter, "Graphene Nanoplatelets/Epoxy Nanocomposites: A Review on Functionalization, Characterization Techniques, Properties, and Applications," *Journal of Reinforced Plastics and Composites* 41 (2022): 99–129, https://doi.org/10.1177/07316844211049277.

22. D. Shelly, V. Singhal, S. Singh, et al., "Exploring the Impact of Nanoclay on Epoxy Nanocomposites: A Comprehensive Review," *Journal of Composites Science* 8 (2024): 506, https://doi.org/10.3390/jcs8120506.

23. H. Y. Pektürk, B. Demir, C. Bilgi, F. Öz, and N. Ersoy, "Effect of MWCNT on the Properties of NCF-CFP Hybrid Composite Fabricated via Vacuum Infusion," *Journal of Reinforced Plastics and Composites* 43 (2024): 1214–1227, https://doi.org/10.1177/07316844231203044.

24. C. Bilgi, B. Demir, H. Aydın, B. Üstün, and Ü. Kurtan, "Effect of Functionalized Graphene Nanoplatelet Dispersion on Thermal and Electrical Properties of Hybrid Carbon Fiber Reinforced Aviation Epoxy Laminated Composite," *Materials Chemistry and Physics* 325 (2024): 129702, https://doi.org/10.1016/j.matchemphys.2024.129702.

25. C. Idumah, "Influence of Morphology and Architecture on Properties and Applications of MXene Polymeric Nanocomposites," *Journal of Thermoplastic Composite Materials* 36 (2023): 4124–4161, https://doi.org/10.1177/08927057221122096.

26. X. Chen, Y. Zhao, L. Li, et al., "MXene/Polymer Nanocomposites: Preparation, Properties, and Applications," *Polymer Reviews* 61 (2021): 80–115, https://doi.org/10.1080/15583724.2020.1729179.

27. C. Bilgi, H. Y. Pektürk, and B. Demir, "Improvement of Mechanical Performance via Interfacial Strengthening of Carbon Fiber-Epoxy Reinforced Hybrid Laminate by Incorporation of Functionalized Graphene Nanoplatelet Interphase," *Polymer Composites* 46 (2025): 4614–4629, https://doi.org/10.1002/pc.29264.

28. L. Gong, I. A. Kinloch, R. J. Young, I. Riaz, R. Jalil, and K. S. Novoselov, "Interfacial Stress Transfer in a Graphene Monolayer Nanocomposite," *Advanced Materials* 22 (2010): 2694–2697, https://doi.org/10.1002/adma.200904264.

29. J. Guest, I. A. Kinloch, and R. J. Young, "The Role of Filler Aspect Ratio in the Reinforcement of an Epoxy Resin With Graphene Nanoplatelets," *Journal of Materials Science* 58 (2023): 9473–9485, https://doi.org/10.1007/s10853-023-08603-3.

30. M. Pawlik, H. Le, and Y. Lu, "Effects of the Graphene Nanoplatelets Reinforced Interphase on Mechanical Properties of Carbon Fibre Reinforced Polymer – A Multiscale Modelling Study," *Composites Part B: Engineering* 177 (2019): 107097, https://doi.org/10.1016/j.compositesb.2019.107097.

31. J. Reif, J. Rafiee, Z. Wang, H. Song, Z.-Z. Yu, and N. Koratkar, "Enhanced Mechanical Properties of Nanocomposites at Low Graphene Content," *ACS Nano* 3 (2009): 3884–3890, https://doi.org/10.1021/nn9010472.

32. S. K. Yadav and J. W. Cho, "Functionalized Graphene Nanoplatelets for Enhanced Mechanical and Thermal Properties of Polyurethane Nanocomposites," *Applied Surface Science* 266 (2013): 360–367, https://doi.org/10.1016/j.apsusc.2012.12.028.

33. J. A. King, D. R. Klimek, I. Miskioglu, and G. M. Odegard, "Mechanical Properties of Graphene Nanoplatelet/Epoxy Composites," *Journal of Composite Materials* 49 (2015): 659–668, https://doi.org/10.1177/0021998314522674.

34. M. Naebe, J. Wang, A. Amini, et al., "Mechanical Property and Structure of Covalent Functionalised Graphene/Epoxy Nanocomposites," *Scientific Reports* 4 (2014): 4375, https://doi.org/10.1038/srep04375.

35. J. Kim, J. Cha, B. Chung, S. Ryu, and S. H. Hong, "Fabrication and Mechanical Properties of Carbon Fiber/Epoxy Nanocomposites Containing High Loadings of Noncovalently Functionalized Graphene Nanoplatelets," *Composites Science and Technology* 192 (2020): 108101, https://doi.org/10.1016/j.compscitech.2020.108101.

36. B. Anasori, M. R. Lukatskaya, and Y. Gogotsi, "2D Metal Carbides and Nitrides (MXenes) for Energy Storage," *Nature Reviews Materials* 2 (2017): 16098, https://doi.org/10.1038/natrevmats.2016.98.

37. M. Naguib, M. Kurtoglu, V. Presser, et al., "Two-Dimensional Nanocrystals Produced by Exfoliation of Ti_3AlC_2," *Advanced Materials* 23 (2011): 4248–4253, https://doi.org/10.1002/adma.201102306.

38. M. Ghidiu, M. R. Lukatskaya, M.-Q. Zhao, Y. Gogotsi, and M. W. Barsoum, "Conductive Two-Dimensional Titanium Carbide 'Clay' With High Volumetric Capacitance," *Nature* 516 (2014): 78–81, https://doi.org/10.1038/nature13970.

39. Y. Sliozberg, J. Andzelm, C. B. Hatter, B. Anasori, Y. Gogotsi, and A. Hall, "Interface Binding and Mechanical Properties of MXene-Epoxy Nanocomposites," *Composites Science and Technology* 192 (2020): 108124, https://doi.org/10.1016/j.compscitech.2020.108124.

40. C. B. Hatter, J. Shah, B. Anasori, and Y. Gogotsi, "Micromechanical Response of Two-Dimensional Transition Metal Carbonitride (MXene) Reinforced Epoxy Composites," *Composites Part B: Engineering* 182 (2020): 107603, https://doi.org/10.1016/j.compositesb.2019.107603.

41. M. Dong, O. Tomes, A. Soul, et al., "Hybrid $Ti_3C_2T_x$ MXene and Carbon Nanotube Reinforced Epoxy Nanocomposites for Self-Sensing and Structural Health Monitoring," *ACS Applied Nano Materials* 7 (2024): 3314–3325, https://doi.org/10.1021/acsanm.3c05728.

42. C. Rong, T. Su, Z. Li, et al., "Elastic Properties and Tensile Strength of 2D Ti3C2Tx MXene Monolayers," *Nature Communications* 15 (2024): 1566, https://doi.org/10.1038/s41467-024-45657-6.

43. A. Raman, J. S. Jayan, B. D. S. Deeraj, M. Srivastava, K. Joseph, and A. Saritha, "Delamination of MXene Using Biomolecule: An Effective Strategy Toward the Utilization of Delaminated MXene as Fillers in Polymer Composites," *Polymer Composites* 46 (2025): 3193–3207, https://doi.org/10.1002/pc.29163.

44. S. Karimi and H. Yahyaei, "Simultaneous Intercalation of Sodium Ion and DMSO Into Ti 3 C 2 MXene /Epoxy With High Electrical Conductivity: Synthesis and Investigation," *Polymer Composites* 46 (2025): 4049–4058, https://doi.org/10.1002/pc.29222.

45. Y. Roohani and H. Yahyaei, "Optimization of EMI Shielding Performance of MXene -Epoxy Nanocomposite Coatings: MXene Loading and Thickness Study," *Polymer Composites* 46 (2025): 8841–8853, https://doi.org/10.1002/pc.29524.

46. M. I. H. Protyai and A. Bin Rashid, "A Comprehensive Overview of Recent Progress in MXene-Based Polymer Composites: Their Fabrication Processes, Advanced Applications, and Prospects," *Heliyon* 10 (2024): e37030, https://doi.org/10.1016/j.heliyon.2024.e37030.

47. J. FitzPatrick and Y. Gogotsi, "MXene Polymer Composites: A Review," *MRS Bulletin* 50 (2025): 1351–1363, https://doi.org/10.1557/s43577-025-00984-x.

48. N. Chu, S.-Y. Lee, Y.-H. Kim, S.-Y. Lee, F.-L. Jin, and S.-J. Park, "Multifunctional MXene/Epoxy Nanocomposites: A Comprehensive Review of Properties, Modifications, and Applications," *Composites. Part A, Applied Science and Manufacturing* 209 (2026): 109932, https://doi.org/10.1016/j.compositesa.2026.109932.

49. K. Vijayananth, S. K. Palaniappan, M. K. Singh, G. Pudhupalayam Muthukutti, S. Mavinkere Rangappa, and S. Siengchin, "Exploring MXene -Polymer Composites for Mechanical, Tribological, and EMI

Shielding Applications," *Polymer Composites* 46 (2025): 16571–16594, https://doi.org/10.1002/pc.70084.

50. A. Akbar, F. N. Bhutto, S. Ali, M. Ali, M. Talha, and L. Lou, "MXenes and Hybrid Composites: Multifunctional Properties, Fabrication Strategies, and Life Cycle Assessment," *Polymer Composites* 47 (2026): 14277–14312, https://doi.org/10.1002/pc.71250.

51. H. Aghamohammadi, N. Amousa, and R. Eslami-Farsani, "Recent Advances in Developing the MXene/Polymer Nanocomposites With Multiple Properties: A Review Study," *Synthetic Metals* 273 (2021): 116695, https://doi.org/10.1016/j.synthmet.2020.116695.

52. B. Ünal, Y. Uslugil, H. Ulus, M. Ekrem, and H. Düzcükoğlu, "MXene-Reinforced Elium Composites: A Comprehensive Study on Tensile and Flexural Strengths, Fracture Toughness, Thermal Properties and Damage Mechanisms," *International Journal of Damage Mechanics* (2026), https://doi.org/10.1177/10567895261465215.

53. A. N. Yuksel Yilmaz, A. C. Bedeloglu, and D. E. Yunus, "The Effect of MXene on the Mechanical and Electromagnetic Interference Shielding Features of Carbon Fabric/Epoxy Scalable Laminated Composites," *Journal of Materials Science* 60 (2025): 7965–7983, https://doi.org/10.1007/s10853-025-10924-4.

54. M. Dong, Y. Hu, H. Zhang, et al., "Micromechanics of Ti3C2Tx MXene Reinforced Poly(Vinyl Alcohol) Nanocomposites," *Composites Part C: Open Access* 13 (2024): 100427, https://doi.org/10.1016/j.jcomc.2023.100427.

55. E. Soroush, P. Afsahi, N. Taheri, H. Hashemi, and B. Ramezanzadeh, "Ti3C2Tx MXene/MoS2 Hybrid Reinforcement of Epoxy Coating for Synergistic Improvement of Thermo-Mechanical, Abrasion and UV-Shielding Performance," *Journal of Materials Research and Technology* 37 (2025): 983–996, https://doi.org/10.1016/j.jmrt.2025.06.054.

56. E. Hajizamani, O. Moini Jazani, and H. Riazi, "MXene -Reinforced Epoxy Adhesives in Structural Bonding: Experimental Investigation and MD Simulations," *Polymer Composites* 46 (2025): 14275–14292, https://doi.org/10.1002/pc.30058.

57. Y. Song, S. Li, Y. Liu, and Y. Zhang, "Heterostructured Three-Dimension MXene/Short Carbon Fiber to Enhance Thermal, Mechanical and Tribological Properties of Epoxy Composites," *Journal of Reinforced Plastics and Composites* 44 (2025): 2396–2406, https://doi.org/10.1177/07316844241256425.

58. M. Berber, A. Haddad, L. Liu, et al., "Wear and Friction Behavior of Wrinkled-Ti 3 C 2 T x/Epoxy Composites," *Journal of Composite Materials* 59 (2025): 159–169, https://doi.org/10.1177/00219983241292770.

59. R. Sanaka, S. K. Sahu, P. S. R. Sreekanth, et al., "Heat-Responsive PLA/PU/MXene Shape Memory Polymer Blend Nanocomposite: Mechanical, Thermal, and Shape Memory Properties," *Polymers* 17 (2025): 338, https://doi.org/10.3390/polym17030338.

60. M. Jing, S. Zhang, S. Zhang, et al., "Low MXene Loading of Epoxy Composite With Enhanced Hydrothermal Resistance," *Polymers* 17 (2025): 1229, https://doi.org/10.3390/polym17091229.

61. ASTM International, *Standard Test Method for Rubber Property Durometer Hardness* (ASTM International, 2021), https://doi.org/10.1520/D2240-15R21.

62. C. Kaykılarlı, H. A. Yeprem, and D. Uzunsoy, "Mechanical and Tribological Characterization of Graphene Nanoplatelets/Al_2O_3 Reinforced Epoxy Hybrid Composites," *Fullerenes, Nanotubes, and Carbon Nanostructures* 31 (2023): 435–447, https://doi.org/10.1080/1536383X.2023.2173740.

63. ASTM International, *Test Method for Tensile Properties of Plastics* (ASTM International, 2022), https://doi.org/10.1520/D0638-22.

64. ASTM International, *Test Methods for Determining the Izod Pendulum Impact Resistance of Plastics* (ASTM International, 2023), https://doi.org/10.1520/D0256-23.

65. A. Iqbal, J. Hong, T. Y. Ko, and C. M. Koo, "Improving Oxidation Stability of 2D MXenes: Synthesis, Storage Media, and Conditions," *Nano Convergence* 8 (2021): 9, https://doi.org/10.1186/s40580-021-00259-6.

66. A. Feng, T. Hou, Z. Jia, Y. Zhang, F. Zhang, and G. Wu, "Preparation and Characterization of Epoxy Resin Filled With Ti3C2Tx MXene Nanosheets With Excellent Electric Conductivity," *Nanomaterials* 10 (2020): 162, https://doi.org/10.3390/nano10010162.

67. M. Soleimani Alavijeh, H. Kefayati, A. Nozad Golikand, and S. Shariati, "Synthesis and Characterization of Epoxy/Graphite/Nano-Copper Nanocomposite for the Fabrication of Bipolar Plate for PEMFCs," *Journal of Nanostructure in Chemistry* 9 (2019): 11–18, https://doi.org/10.1007/s40097-019-0293-x.

68. J. Orellana, E. Araya-Hermosilla, A. Pucci, and R. Araya-Hermosilla, "Polymer-Assisted Graphite Exfoliation: Advancing Nanostructure Preparation and Multifunctional Composites," *Polymers* 16 (2024): 2273, https://doi.org/10.3390/polym16162273.

69. T. Watanabe and M. Yasuda, "Fracture Behaviour of Sheet Moulding Compounds. Part 1. Under Tensile Load," *Composites* 13 (1982): 54–58, https://doi.org/10.1016/0010-4361(82)90171-9.

70. M. Shirinbayan, A. Abdessalem, A. Kallel, S. Nouira, A. M. Laribi, and J. Fitoussi, "Viscoelastic-Damageable Behavior of Sheet Molding Compound (SMC) Composites," *Polymers and Polymer Composites* 32 (2024), https://doi.org/10.1177/09673911241275594.

71. Y. Dobah, M. Bourchak, A. Bezazi, A. Belaadi, and F. Scarpa, "Multi-Axial Mechanical Characterization of Jute Fiber/Polyester Composite Materials," *Composites Part B: Engineering* 90 (2016): 450–456, https://doi.org/10.1016/j.compositesb.2015.10.030.

72. K. Y. Eayal Awwad, B. F. Yousif, K. Fallahnezhad, K. Saleh, and X. Zeng, "Influence of Graphene Nanoplatelets on Mechanical Properties and Adhesive Wear Performance of Epoxy-Based Composites," *Friction* 9 (2021): 856–875, https://doi.org/10.1007/s40544-020-0453-5.

73. P.-C. Chuang, C. Yu Chao, M. Yang, and J.-L. Tsai, "Investigating Fracture Toughness of Graphene Epoxy Nanocomposites Using Single Edge Notched Bending Specimens," *Journal of Mechanics* 39 (2023): 105–112, https://doi.org/10.1093/jom/ufad007.

74. M. Alsaadi, B. Younus, A. Erklig, M. Bulut, O. Bozkurt, and B. Sulaiman, "Effect of Graphene Nano-Platelets on Mechanical and Impact Characteristics of Carbon/Kevlar Reinforced Epoxy Hybrid Nanocomposites," *Proceedings of the Institution of Mechanical Engineers, Part C: Journal of Mechanical Engineering Science* 235 (2021): 7139–7151, https://doi.org/10.1177/09544062211016883.

75. A. Tanvir, P. Sobolčiak, A. Popelka, et al., "Electrically Conductive, Transparent Polymeric Nanocomposites Modified by 2D $Ti_3C_2T_x$ (MXene)," *Polymers* 11 (2019): 1272, https://doi.org/10.3390/polym11081272.

76. R. Liu and W. Li, "High-Thermal-Stability and High-Thermal-Conductivity $Ti_3C_2T_x$ MXene/Poly(Vinyl Alcohol) (PVA) Composites," *ACS Omega* 3 (2018): 2609–2617, https://doi.org/10.1021/acsomega.7b02001.

77. L. Liu, G. Ying, D. Wen, et al., "Aqueous Solution-Processed MXene (Ti3C2Tx) for Non-Hydrophilic Epoxy Resin-Based Composites With Enhanced Mechanical and Physical Properties," *Materials and Design* 197 (2021): 109276, https://doi.org/10.1016/j.matdes.2020.109276.

78. R. Wazalwar, M. Tripathi, and A. M. Raichur, "Curing Behavior and Mechanical Properties of Tetra-Functional Epoxy Reinforced With Polyethyleneimine-Functionalized MXene," *ACS Applied Polymer Materials* 4 (2022): 2573–2584, https://doi.org/10.1021/acsapm.1c01876.

79. L. Liu, G. Ying, C. Hu, et al., "Functionalization With MXene (Ti 3 C2) Enhances the Wettability and Shear Strength of Carbon Fiber-Epoxy Composites," *ACS Applied Nano Materials* 2 (2019): 5553–5562, https://doi.org/10.1021/acsanm.9b01127.

80. M. Dong, Y. Hu, X. Yu, et al., "Probing Interfacial Interactions in Ternary Nanocomposites of Ti 3 C 2 T x MXene Nanoplatelets, Multi-walled Carbon Nanotubes, and Poly(Vinyl Alcohol) Toward Synergistic Reinforcement," *ACS Applied Polymer Materials* 6 (2024): 207–217, https://doi.org/10.1021/acsapm.3c01816.

81. S. M. Naqvi, T. Hassan, A. Iqbal, et al., "Surface Functionalization of $Ti_3C_2T_x$ MXenes in Epoxy Nanocomposites: Enhancing Conductivity, EMI Shielding, Thermal Conductivity, and Mechanical Strength," *ACS Applied Materials & Interfaces* 17 (2025): 20149–20161, https://doi.org/10.1021/acsami.4c21997.